2018

Boosting the Potassium Storage Performance of Alloy-Based Anode Materials via Electrolyte Salt Chemistry

Qing Zhang
University of Wollongong, qz964@uowmail.edu.au

Jianfeng Mao
University of Wollongong, jmao@uow.edu.au

Wei Kong Pang
University of Wollongong, wkpang@uow.edu.au

Tian Zheng
University of Wollongong, tz648@uowmail.edu.au

Vitor Sencadas
University of Wollongong, victors@uow.edu.au

See next page for additional authors

Boosting the Potassium Storage Performance of Alloy-Based Anode Materials via Electrolyte Salt Chemistry

Abstract

Potassium-ion batteries (PIBs) are promising energy storage systems because of the abundance and low cost of potassium. The formidable challenge is to develop suitable electrode materials and electrolytes for accommodating the relatively large size and high activity of potassium. Herein, Bi-based materials are reported as novel anodes for PIBs. Nanostructural design and proper selection of the electrolyte salt have been used to achieve excellent cycling performance. It is found that the potassiation of Bi undergoes a solid-solution reaction, followed by two typical two-phase reactions, corresponding to $Bi \leftrightarrow Bi(K)$ and $Bi(K) \leftrightarrow K_5Bi_4 \leftrightarrow K_3Bi$, respectively. By choosing potassium bis(fluorosulfonyl)imide (KFSI) to replace potassium hexafluorophosphate (KPF_6) in carbonate electrolyte, a more stable solid electrolyte interphase layer is achieved and results in notably enhanced electrochemical performance. More importantly, the KFSI salt is very versatile and can significantly promote the electrochemical performance of other alloy-based anode materials, such as Sn and Sb.

Disciplines

Engineering | Physical Sciences and Mathematics

Authors

Qing Zhang, Jianfeng Mao, Wei Kong Pang, Tian Zheng, Vitor Sencadas, Yuanzhen Chen, Yajie Liu, and Zaiping Guo

Boosting the potassium storage performance of Alloy-based anode materials via electrolyte salt chemistry

Qing Zhang, Jianfeng Mao*, Wei Kong Pang, Tian Zheng, Vitor Sencadas, Yuanzhen Chen, Yajie Liu and Zaiping Guo*

Qing Zhang, Dr. Jianfeng Mao*, Dr. Wei Kong Pang, Dr. Yuanzhen Chen, Yajie Liu and Prof. Zaiping Guo*
Institute for Superconducting & Electronic Materials, University of Wollongong, Wollongong, NSW 2522, Australia.
E-mail: jmao@uow.edu.au, zguo@uow.edu.au

Dr. Tian Zheng

Intelligent Polymer Research Institute, University of Wollongong, Wollongong, NSW 2522, Australia.

Dr. Vitor Sencadas

School of Mechanical, Materials, Mechatronics & Biomedical Engineering, University of Wollongong, NSW 2500, Australia.

Prof. Zaiping Guo

School of Mechanical, Materials, Mechatronics & Biomedical Engineering, University of Wollongong, NSW 2500, Australia.

Abstract

Potassium-ion batteries (PIBs) are promising energy storage systems because of the abundance and low cost of potassium. The formidable challenge is to develop suitable electrode materials and electrolytes for accommodating the relatively large size and high activity of potassium. Herein, we report Bi-based materials as novel anodes for PIBs. Nanostructural design and proper selection of the electrolyte salt have been used to achieve excellent cycling performance. It was found that the potassiation of Bi undergoes a solid-solution reaction, followed by two typical two-phase reactions, corresponding to Bi$\leftrightarrow$ Bi(K)

and Bi(K) $\leftrightarrow$ K_5Bi_4 $\leftrightarrow$ K_3Bi, respectively. By choosing potassium bis(fluorosulfonyl)imide (KFSI) to replace potassium hexafluorophosphate (KPF_6) in carbonate electrolyte, a more stable solid electrolyte interphase (SEI) layer has been achieved and results in notably enhanced electrochemical performance. More importantly, the KFSI salt is very versatile and can significantly promote the electrochemical performance of other alloy-based anode materials such as Sn and Sb.

1. Introduction

Owing to the rapid growth in use of renewable energy resources such as the sun and the wind, low-cost and high-performance energy storage devices are urgently needed to efficiently use these intermittent energy sources and reduce our energy dependence on fossil fuels. Lithium-ion batteries (LIBs) are widely used in portable electronic devices, and have been used in (hybrid) electric vehicles, and even in grid-scale facilities.[1,2] Nevertheless, concerns about LIBs have arisen due to their high cost, the limited nature of lithium resources in the Earth's crust (0.0017 wt%), and their uneven distribution.[3,4] Hence, it is essential to search for alternative energy storage technologies based on the low-cost and abundant elements, i.e. sodium or potassium.[5-10]

Potassium-ion batteries (PIBs) have been attracting research interest due to the low cost and abundance (2.09 wt% in the Earth's crust) of potassium resources, and the similar physical and chemical properties of K to Li and Na.[8-10] Several advantages of PIBs have already been demonstrated compared to sodium or lithium ion batteries. The standard electrochemical potential of K/K$^+$ (-2.93 V vs. $E°$) is lower than for Na/Na$^+$ (-2.71 V vs. $E°$), and close to that for Li/Li$^+$ (-3.04 V vs. $E°$), but the lowest redox potential is also found in some solvents such as propylene carbonate (PC) and ethylene carbonate/diethyl carbonate (EC/DEC) due to the

relatively lower desolvation energy of K^+ in organic solvents, indicating that PIBs may offer a higher working voltage and more energy.[11,12] The weaker Lewis acidity of K ions with organic solvents also enables fast kinetics and high rate capability.[12,13] In addition, the potential gap of some carbon and metal based anodes in PIBs has been found to be higher than in sodium-ion batteries (SIBs), which leads a lower risk of short-circuiting due to dendrite growth.[14,15] Therefore, PIBs can be expected as an alternative to SIBs or even LIBs.[11-35]

For the success of PIBs, one key strategy is to develop feasible electrode materials that can accommodate the large sized K^+ ion (1.38 Å), which is bigger than for Li^+ (0.76 Å) and Na^+ (1.02 Å). For the anode, carbonaceous materials,[16-21] organic materials,[22,23] K-ion intercalation compounds,[24-28] and metal-based alloy materials[29-32] have all been investigated. The capacities for the former three kinds of anodes are relatively low (< 300 mAh g^{-1}), however. The latter metal-based materials have larger capacities, but capacity fading has always been observed due to the continuous pulverization resulting from the large volume expansion and contraction. Another key strategy is to achieve a stable solid electrolyte interphase (SEI) layer. It is well-known that SEI layers are strongly dependent on the salt and solvent of the electrolyte, and they play an important role in maintaining the electrochemical performance of rechargeable batteries such as LIBs and SIBs.[36,37] The SEI layer is even more important for PIBs due to the higher chemical reactivity of K compare to Li or Na. It has been reported that more stable SEI layers can be obtained in ether based electrolytes,[22,35] but ethers may be not suitable for a full battery, as they are easily oxidised at high potential. It is well known that ethers have seldom been considered suitable as solvents for LIBs because of their instability on 4 V class cathode surfaces.[38] In carbonate based electrolytes, it was also reported that higher conductivity and less side reactions could be achieved by using potassium bis(fluorosulfonyl)imide (KFSI) salt instead of using

potassium hexafluorophosphate (KPF$_6$) salt in the carbon-based anodes,[11,39] although the mechanism for the action of different potassium salts on the SEI formation is not clear yet. Also, there has been limited exploration on the formation of the SEI layer for K$^+$ storage materials.

Bismuth is a well-known "green" metal with low cost and a nontoxic nature, and it is also of interest for electronic applications due to its unique properties, such as its low melting point, and very low thermal conductivity and volume expansion compared to other metals upon freezing. More significantly, Bi has a unique layered crystal structure with large interlayer spacing along the *c*-axis, $d(003) = 3.95$ Å, which makes it very promising as a potential anode material for rechargeable batteries.[40-45] In this work, we report Bi-based materials as novel potential anodes for K-ion batteries, and the reaction mechanism is investigated and proposed. The Bi nanoparticles are confined on the graphene nanosheets to form a Bi/ reduced graphene oxide (Bi/rGO) nanocomposite for achieving better electrochemical performance, since graphene is an electrical conductor and a good substrate for buffering the volume changes in Bi nanoparticles during electrochemical cycling. We also discovered that KFSI outperforms KPF$_6$ and leads to Bi anodes with significantly improved cycling stability when used as the salt in nonaqueous carbonate solvents. The interfacial chemistry during cycling was investigated by scanning and transmission electron microscopy (SEM and TEM), X-ray photoelectron spectroscopy (XPS), Kelvin probe force microscopy (KPFM), and nanoindentation. It is shown that the nature of the salt has a significant influence on the uniformity, stability, and chemical composition of the SEI. As a result, the Bi anodes in KFSI can survive over 200 cycles, which is the longest-cycled metal-based anode in PIBs that has been firstly reported. Moreover, since the alloy-based anode materials experience similar issues resulting from the huge volume changes during potassiation and depotassiation

process, the proposed KFSI salt can also be applied with other alloy-based anodes such as Sn/C and Sb/C to enhance their potassium storage properties.
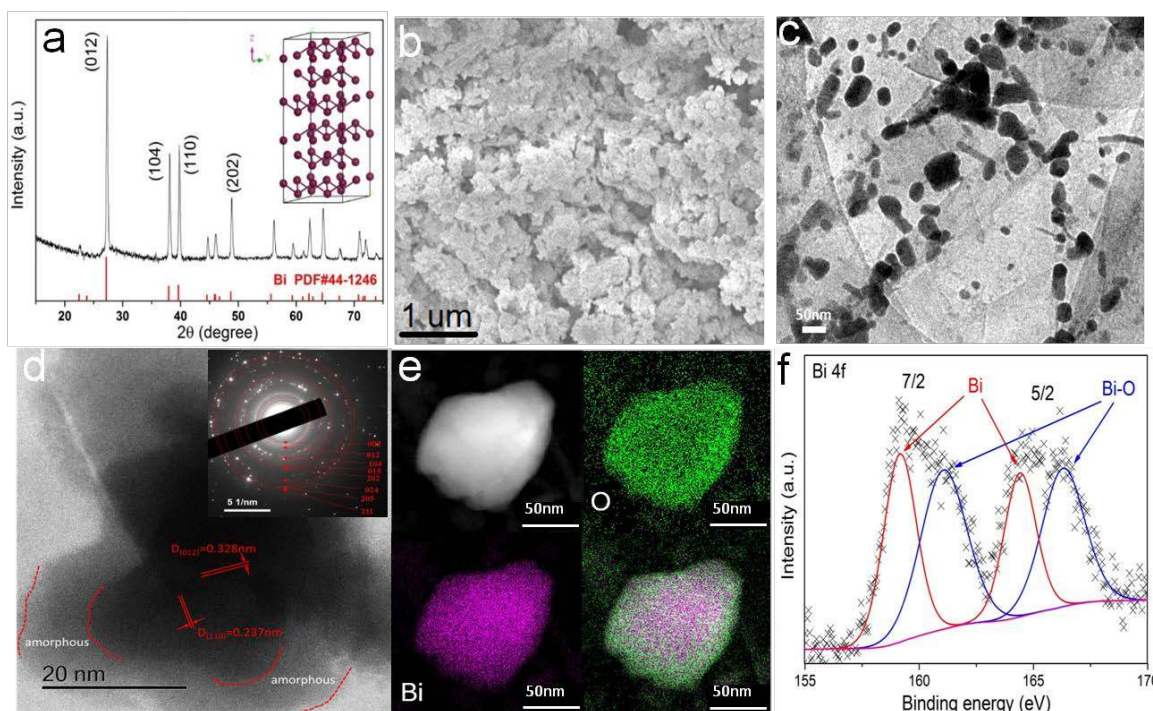
2. Results and discussion

Figure 1. Physical properties of as-synthesized Bi/rGO. a) XRD pattern, with the inset showing the crystal structure of the hexagonal Bi; b) SEM image; c) Low resolution TEM image; d) High resolution TEM image with inset SAED pattern; e) EDS maps; f) XPS spectrum of Bi peaks.

2.1 Materials synthesis and characterization.

Bi/rGO nanocomposite was synthesized via a simple room-temperature solution synthesis method. The crystallinity and phase composition of the Bi/rGO were investigated by X-ray diffraction (XRD). As shown in **Figure. 1** (a), all the diffraction peaks can be indexed to hexagonal Bi with space group $R\bar{3}m$ (PDF no. 44-1246). The hexagonal layered crystal structure of Bi is shown in the inset of Figure. 1(a). The presence of rGO in the composite can be confirmed by the Raman spectrum, as shown in Figure. S1 in the Supporting Information. The morphology of Bi/rGO, as captured by SEM (Figure. 1(b)) and TEM

(Figure. 1(c)), reveals that the Bi nanoparticles with 30-100 nm in size are <mark>properly</mark> dispersed on the graphene nanosheets. In contrast, the pristine Bi particles in the reference sample are aggregated (Figure. S2). The presence of rGO can not only mitigate the agglomeration of Bi nanoparticles, but also improves the electrical conductivity and structural stability of the electrode. The well-defined crystallinity of Bi in the Bi/rGO nanocomposite is further confirmed by the high resolution TEM (HRTEM) image and selected area electron diffraction (SAED) pattern shown in Figure. 1(d), although a clear amorphous layer surrounding the crystallized region of Bi is also observed. The energy dispersive spectroscopy (EDS) mapping of the Bi particle in Figure. 1(e) illustrates the Bi core and the amorphous Bi_2O_3 shell resulting from the oxidation of Bi in the core-shell Bi_2O_3@Bi composite. The presence of Bi_2O_3 is also confirmed by the XPS spectrum (Figure. 1(f)), where the ratio of Bi-Bi to Bi-O bonds is found to be 1.2:1. Based on the XPS results, as well as the thermogravimetric (TG) measurements (Figure. S3), the weight ratio between Bi, Bi_2O_3, and rGO in the Bi/rGO composite was determined to be 51.1:47.5:1.4. This result is understandable, as Bi is easily oxidized upon contact with air, and hence, a surface amorphous layer surrounding the Bi particle is present.
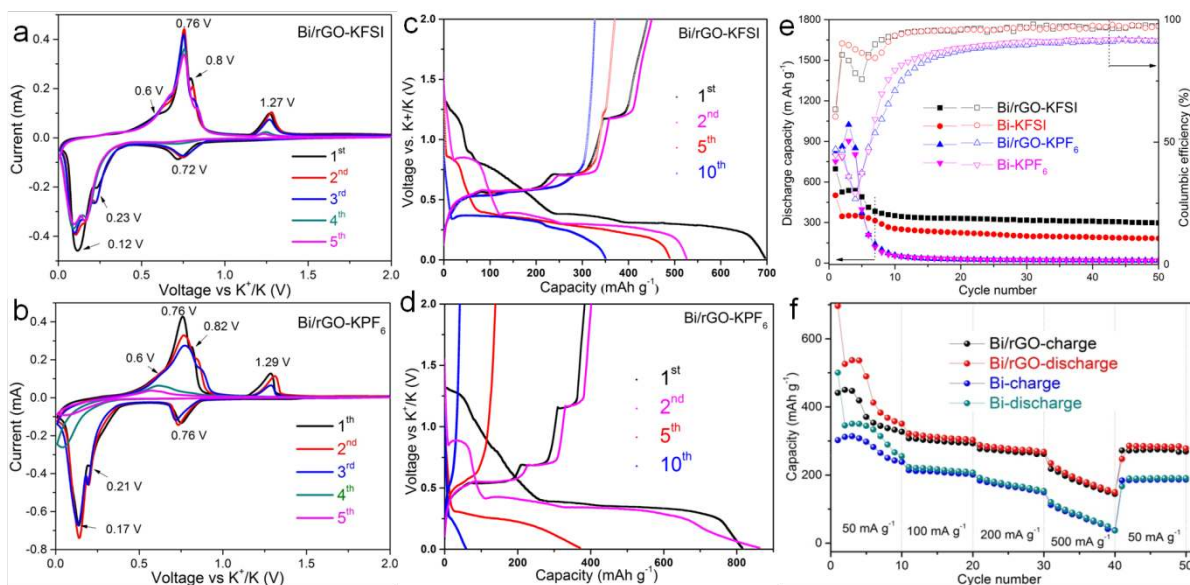
Figure 2. Electrochemical performance of Bi-based electrodes for K storage. Cyclic voltammograms (CVs) for the first 5 cycles of Bi/rGO in (a) KFSI electrolyte and (b) KPF$_6$ electrolyte at a scanning rate of 0.05 mV s^{-1}. Galvanostatic discharge–charge profiles for selected cycles of the Bi/rGO in (c) KFSI electrolyte and (d) KPF$_6$ electrolyte at 50 mA g^{-1}. (e) Cycling performance of Bi and Bi/rGO electrodes in KPF$_6$ and KFSI electrolytes at 50 mA g^{-1} and the corresponding Coulombic efficiency. (f) Rate capabilities of Bi and Bi/rGO in KFSI electrolyte at various current densities.

2.2 Potassium storage performance.

The electrochemical performance of the Bi/rGO electrode in both the KPF$_6$ and KFSI electrolytes was first evaluated by cyclic voltammetry (CV), as shown in **Figure. 2** (a, b). The CVs for commercial Bi$_2$O$_3$ and carbon black are also presented for comparison, as shown in Figure. S4. As expected, both the Bi/rGO and Bi$_2$O$_3$ electrodes in KFSI electrolyte show similar reduction/oxidation pairs, since there is an amorphous Bi$_2$O$_3$ layer covering the Bi particles in the Bi/rGO sample. During the initial scan, a first reduction peak at 0.72 V and its corresponding oxidation peak at about 1.29 V were observed, which may reflect the conversion reaction of Bi$_2$O$_3$ and possible intercalation of Bi. The redox peak at 0.72/1.29 almost disappeared after only 5 cycles, however, suggesting its irreversibility. Upon further potassiation, a large reduction peak was observed at about 0.12 V and a small shoulder at about 0.23 V due to the alloying of K$^+$ with Bi, although the large reduction peak splits into two peaks at 0.16 and 0.1 V after the first cathodic scan. In the anodic scan, a large oxidation

peak at 0.76 V and two small shoulders at 0.6 and 0.82 V were observed, which may be associated with the extraction of potassium from the K-Bi phase. The results suggest that the electrochemical K ion insertion/ extraction reaction of Bi may take place via multiple steps. The Bi/rGO in KPF_6 electrolyte shows similar electrochemical behaviour, but all the cathodic and anodic peaks for the Bi/rGO in KPF_6 electrolyte almost disappear from the fifth scan onward (Figure. 2(b)), suggesting bad cycling performance. In contrast, the CV curves of the Bi/rGO in KFSI electrolyte show good reversibility in the insertion/extraction reactions of K into/out of Bi.

Galvanostatic discharge/charge measurements were also conducted to evaluate the electrochemical performance of the Bi anodes. Remarkably, the Bi anodes showed significantly enhanced electrochemical performance in KFSI electrolyte compared to the KPF_6 electrolyte (Figure. 2, Figure. S5-S7). The Bi/rGO electrode delivered a high reversible capacity of 441 mA h g^{-1} with an initial coulombic efficiency (CE) of 63% in KFSI electrolyte (Figure. 2(c, e)). In contrast, it had a lower reversible capacity of 384 mA h g^{-1} with a much lower initial CE of 47 % in KPF_6 electrolyte (Figure. 2(d, e)). In both of KFSI and KPF_6 electrolytes, the initial CE is under 70% which is due to the side-actions of the growth of SEI layer, as well as the irreversible conversion reaction from the reducing of Bi_2O_3 to Bi. Furthermore, both the Bi and Bi/rGO anodes in KPF_6 electrolyte experienced an abrupt capacity drop after only 4 cycles (Figure. 2(e)). In contrast, both the Bi and the Bi/rGO anodes in KFSI electrolyte showed stable cycling performance up to 50 cycles and delivered reversible capacities of 177 and 290 mAh g^{-1} after 50 cycles, respectively (Figure. 2(e)). In particular, the Bi/rGO can still maintain its electrochemical activity even after 200 cycles (Figure. S7). It should be noted that both the Bi and the Bi/rGO in KFSI electrolyte are relatively stable in the initial cycles and then experience relatively fast capacity fading in the following several cycles, which is due to the irreversible conversion reaction, according to

the CV curve and discharge/charge curves. After the disappearance of Bi_2O_3, the Bi anodes show relatively stable capacity, and the coulombic efficiency in the KFSI electrolyte can be maintained in the range of 97-98% (Figure. 2(e)). The Bi/rGO electrodes also exhibited an impressive rate capability in the KFSI electrolyte. As shown in Figure. 2(f), the Bi/rGO electrode delivered a reversible capacity of 309, 273, and 235 mAh g^{-1} at the current densities of 100, 200, and 500 mA g^{-1}, respectively, which are significantly higher than for the pristine Bi electrode. When the current rate was set back to 50 mA g^{-1}, a reversible capacity of about 274 mAh g^{-1} was obtained, demonstrating good rate capability. The electrochemical performance of Bi/rGO anode is better than for most other reported anodes (Table S1). In particular, the Bi/rGO shows higher rate capacities than the carbon based anodes and is the best metal based anode reported so far that could last for over 200 cycles. The excellent reversibility and capacity retention of the electrode in the KFSI electrolyte indicates that KFSI is very useful for reducing the irreversible capacity and improving the cycle life. In addition, graphene provides effective electron conduction paths, and the network-like structure of graphene nanosheets forms a stable matrix for the Bi electrode. We also tried to optimize the performance of the Bi/rGO by tuning the compositions of the KFSI and KPF_6 salts or the solvent. As shown in Figure. S7a, the addition of 0.2 M KPF_6 into the 0.8 M KFSI electrolyte can increase the capacity, while more KPF_6 addition (0.5 and 0.7 M) will reduce the capacity. Nevertheless, the best cycling performance is still obtained from the pristine KFSI electrolyte. Also, better electrochemical performance can be obtained with KFSI salt by using EC/DEC solvent to replace EC/ dimethyl carbonate (DMC) (Figure. S7b). The cut-off voltage also plays a key role in achieving better cycling performance. The capacity was increased from 87 to 120 mAh g^{-1} after 200 cycles at 50 mA g^{-1} when the voltage window was reduced from 0.01-2 V to 0.01-1 V (Figure. S7c).
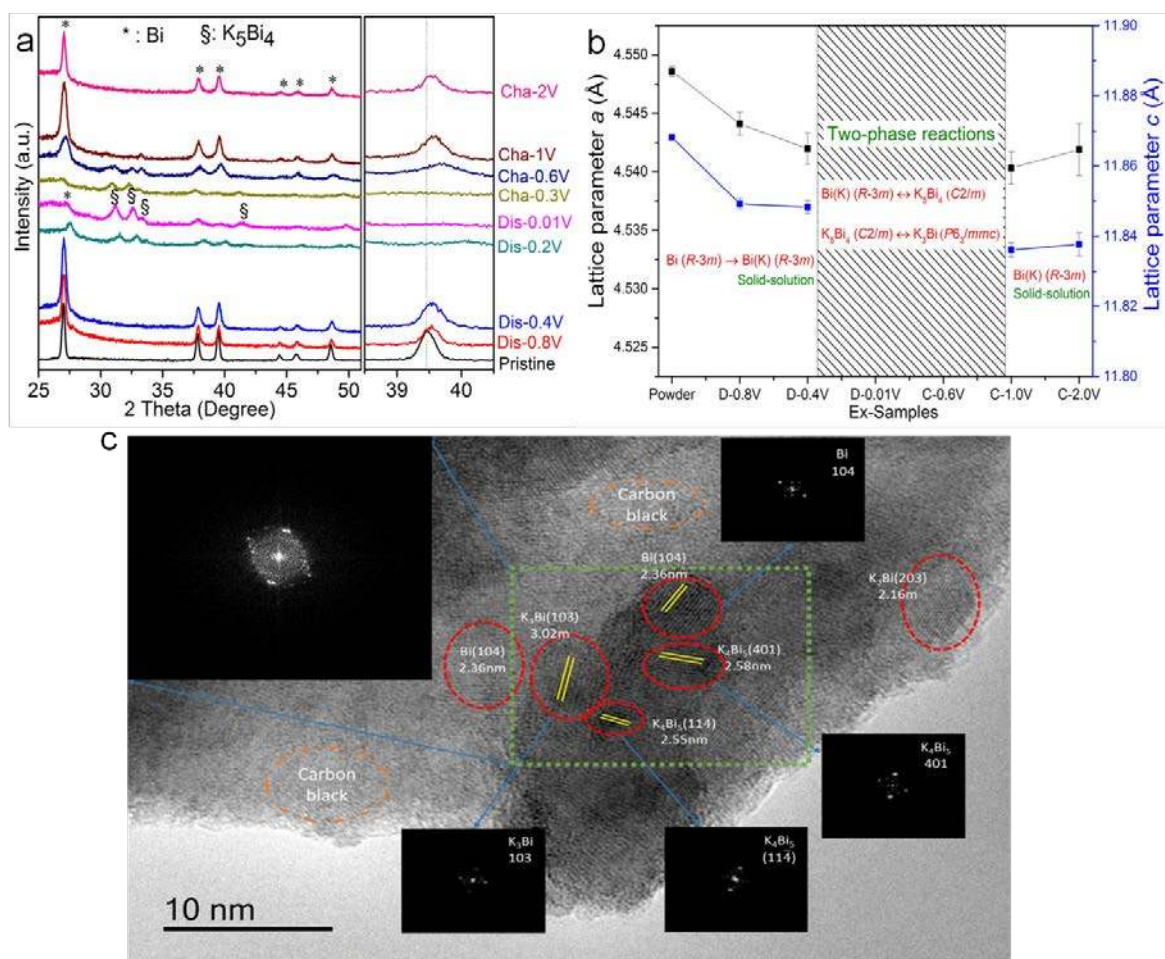
Figure 3. Potassium-storage mechanism of Bi. (a) Ex-situ XRD patterns collected at different points in the discharge/charge cycle; (b) The refined lattice parameters and proposed potassiation/depotassiation mechanism; and (c) TEM image with inset images showing fast Fourier transform patterns of selected areas of a Bi@rGO electrode after it was fully discharged.

2.3 Potassium storage mechanism.

To understand the potassium-storage mechanism, ex-situ XRD and TEM measurements were performed on Bi/rGO electrodes that were disassembled at various voltages. **Figure. 3** (a) shows the ex-situ XRD patterns of the selected discharge and charge states. As discussed above, the Bi/rGO sample has amorphous Bi_2O_3 layers on the surfaces of the Bi particles, and the Bi/rGO will undergo conversion reactions during discharge ($Bi_2O_3 + 6K^+ + 6e^- \rightarrow 2Bi + 3K_2O$). No XRD signals from the K_2O phase are detected, however, due to the possible amorphous state. Upon discharge to 0.4 V, all the reflections of Bi remain, but with

their peak positions slightly shifted to higher detection angle 2θ, indicating that the lattice parameters (a, c) of Bi phase become smaller, as estimated by Rietveld analysis and shown in Figure. 3(b). This lattice shrinkage implies that Bi undergoes a solid-solution reaction and forms a Bi(K) solid-solution phase with the same symmetry. The observation of lattice shrinkage as a consequence of K intercalation is similar to the reported sodiation mechanism of Bi.[41] Although no reasons for lattice shrinkage were given in the previous work on sodium ion batteries, we believe that the lattice shrinkage is due to the inserted K ions, which are allocated to interstitial sites between the Bi layers within the R-3m structure, reducing the repulsion force between Bi layers. Upon further discharge to 0.2 and 0.01 V, we found that the Bi(K) structure cannot tolerate extra K intercalation and is transformed into the K_5Bi_4 phase, with the Bi(K) reflection intensity decreasing and that of K_5Bi_4 increasing through a two-phase reaction. Upon charge, the two-phase reaction is reversed, with the K_5Bi_4 disappearing and the Bi(K) coming back. Lattice expansion of Bi(K) was also observed during the K extraction due to the partially reversed solid-solution reaction. Considering the fact that the Bi/rGO has several redox pairs and delivers a capacity of over 300 mAh g^{-1}, much higher than the theoretical capacity of 160 mAh g^{-1} for K_5Bi_4, a K-rich phase should be present upon full discharge. As shown in Figure. 3(c), in addition to Bi and K_5Bi_4, the HRTEM and corresponding fast Fourier transform (FFT) images of selected areas present the characteristic diffraction points of K_3Bi, which is not detected by XRD due to its possible nanocrystalline nature and low amount. The K_3Bi is likely to be the final product after the discharge of the Bi/rGO electrode to 0.01 V in PIBs, with the theoretical capacity being as high as 385 mA h g^{-1}. Therefore, the ex-situ XRD and TEM results jointly suggest the presence of two typical two-phase reactions corresponding to Bi(K) $\leftrightarrow K_5Bi_4 \leftrightarrow K_3Bi$, as shown in Figure. 3(b). The volume expansion of per unit Bi upon 3 K intercalation (K_3Bi) is as large as 515.23%. [46-48] Overall, the potassiation/depotassiation of Bi proceeds through an

alloying/dealloying reaction mechanism with K with solid-solution and two-phase reactions,

and is highly reversible.
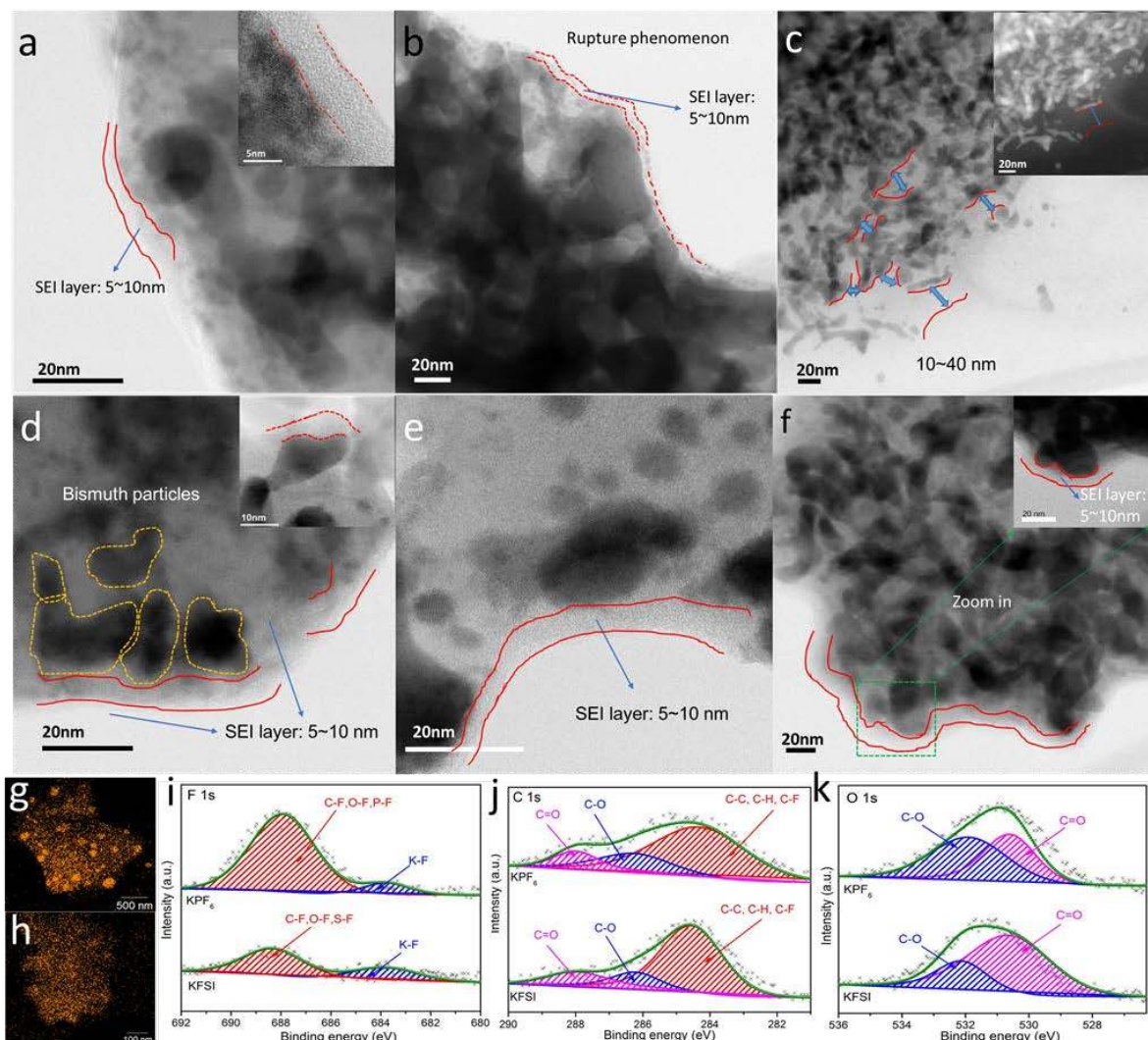
Figure 4. Ex-situ TEM images of Bi/rGO electrode after 2 cycles, 5 cycles, and 10 cycles in KFP_6 (a, b, c) and KFSI (d, e, f) electrolytes, with the insets showing higher magnification. EDS maps of F element in Bi/rGO electrode after 10 cycles in (g) KPF_6 and (h) KFSI electrolytes. XPS surface analysis for (i) F 1s, (j) C 1s, and (k) O 1s of Bi/rGO electrode after 10 cycles in KPF_6 and KFSI electrolytes, respectively.

2.4 Surface chemistries.

To understand how the KFSI salt could greatly enhance the cycling performance, Bi/rGO

electrodes cycled in both KFSI and KPF_6 electrolytes were carefully characterized. **Figure.**

4(a-f) shows HRTEM images of electrodes after cycling in both electrolytes. The thickness of

the SEI layer (5-10 nm) in the two electrolytes is similar after two cycles as shown in Figure. 4 (a, d), although obvious differences are observed upon further cycling (Figure. 4(b, c, e, f)). In KPF_6 electrolyte, the SEI layer was found to be ruptured, and crevices were detected on the surface of the SEI layer after 5 cycles (Figures. 4(b), S8), which was due to the pulverization of Bi nanoparticles, which breaks the SEI layer due to the huge volume changes in the Bi nanoparticles during discharge/charge. This will produce new Bi surface, which will be exposed to the electrolyte and lead to further irreversible decomposition of the electrolyte and new growth of the SEI layer. As a result, thicker and more heterogeneous SEI layers (10-30 nm) were formed after 10 cycles (Figure. 4(c)), leading to the continuous consumption of electrolyte. In contrast, the SEI layer formed in KFSI electrolyte maintained its integrity and showed a similar thickness from 2 to 10 cycles (Figure. 4(d-f)), indicating that the SEI layer in KFSI electrolyte is much more stable and could prevent the continuous side reactions between the electrolyte and the electrode. The results were further confirmed by the ex-situ SEM results, as shown in Figure. S9. The 10th cycle electrode in KPF_6 electrolyte exhibits surface destruction with nonhomogeneous SEI coverage. In contrast, after the 10th cycle, the electrode in KFSI electrolyte remains homogeneous and keeps its integrity, with the compact SEI layer uniformly covering the particles.

EDS mapping shows that the SEI layers in the two electrolytes consist of different elements, as shown in Figure. S10. Besides the shared elements Bi, C, and O that arise from the electrode and solvent, three additional elements, F, P, and K, were detected for the electrode in KPF_6, and four additional elements, F, N, S, and K, were detected for the electrode in KFSI electrolyte. From the EDS mapping images, it was also observed that the elemental distributions, in particular the F and P distributions, on the electrode surface in KFSI is more uniform than in the KPF_6 electrolyte (Figures. 4(g, h), S10). The chemical compositions of the SEI in the KPF_6 and KFSI electrolytes were also analysed by XPS, as shown in Figure.

4(i-k). The F 1s spectra reveal two similar peaks for both electrolytes in the range of 685-692 eV and at 684.0 eV (Figure. 4(i)). The feature at 685-692 eV can be assigned to S-F species in the KFSI electrolyte and P-F species in the KPF_6 electrolyte, respectively, due to incomplete decomposition of the salts. The second one at 684.0 eV is attributed to the KF species. The formation of KF in KPF_6 electrolyte is possible from the direct decomposition of the salt ($KPF_6 \rightarrow KF + PF_5$), hydrolysis of the salt ($KPF_6 + H_2O \rightarrow KF + 2HF + POF_3$), and/or reactions of the potassium containing compounds with Lewis acids (e.g. HF, POF_3, PF_5) derived from KPF_6.[38] In contrast, the KF found in KFSI electrolyte may be from the reduction of S-F bonds in the FSI^-.[35] The presence of strong Lewis acids (e.g. HF, POF_3, PF_5) derived from KPF_6 not only induces the polymerization of EC solvent,[38, 49-51] but may also induce a reaction with the particle surface (e.g. K_2O).[39] KFSI is less sensitive toward hydrolysis compared to KPF_6, and hence, the use of KFSI could prevent the formation of strong Lewis acids. In contrast, KFSI appears to be more easily reducible than KPF_6 at the surface of the electrode.[51] In the C 1s spectrum (Figure. 4(j)), both the C-O and C=O species in the surface layer are detected in both the KPF_6 and the KFSI, which may have originated from the decomposition of the carbonate solvent. The O 1s signals also suggest the co-existence of C-O and C=O in both the KPF_6 and the KFSI (Figure. 4(k)). This indicates that both organic (e.g. CH_3OK) and inorganic (e.g. K_2CO_3) components may be present, but they may be different in their relative proportions.[52,53] In addition, some other oxide species may also be present in KFSI, since the O 1s peak of 532.5 eV can also be assigned to S=O.[35] Therefore, the growth mechanism of the SEI layer in the two electrolytes is very different, due to the usage of different salts, where the SEI layer formed in KPF_6-based electrolytes is mainly from solvent-induced reduction, while the one in KFSI originates predominantly from salt reduction.
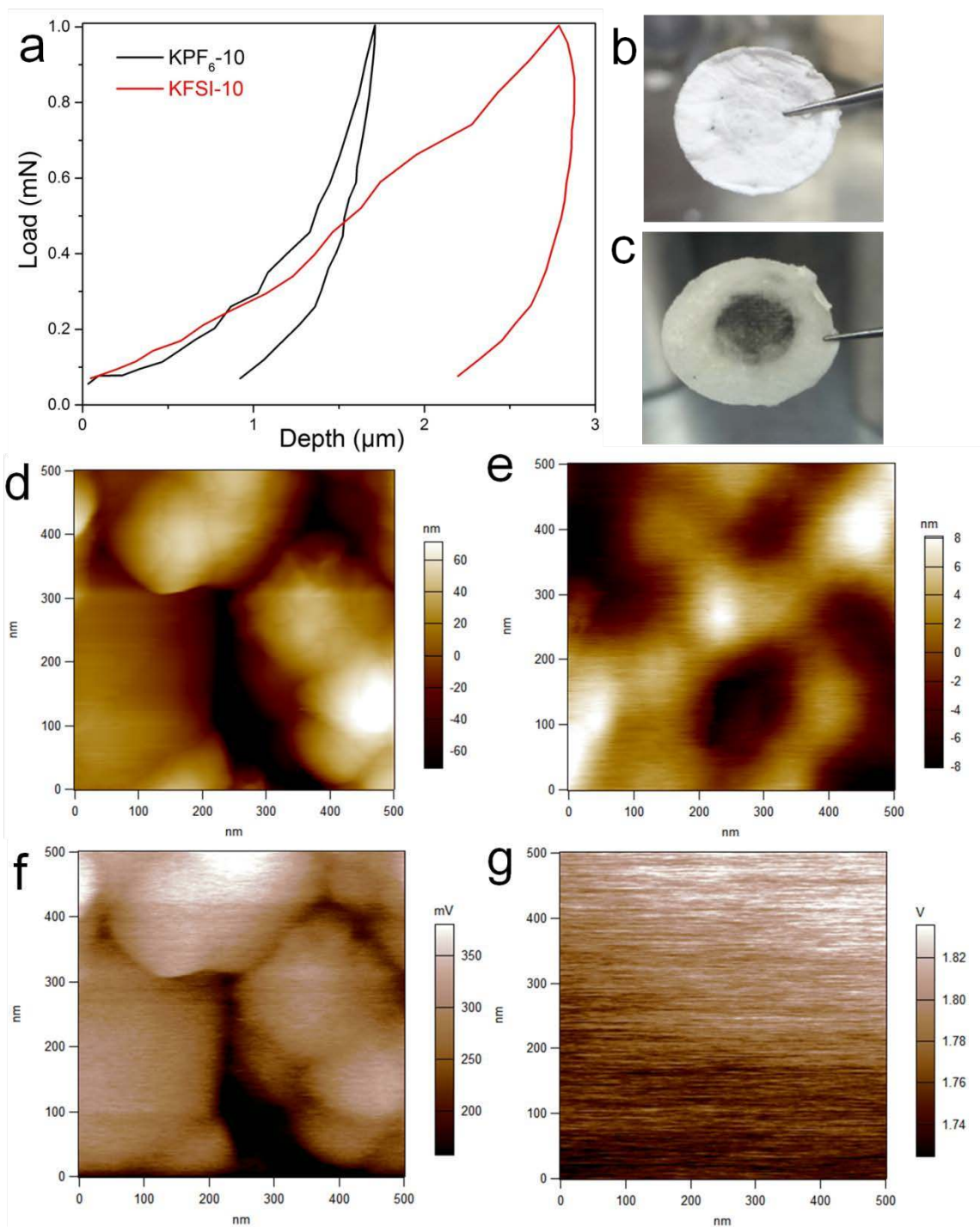
Figure 5. (a) Nanoindentation force of the Bi/rGO electrode at a given indentation depth after cycling in KPF_6 and KFSI electrolyte, respectively. Digital photographs of the separator after 10 cycles in (b) KFSI electrolyte and (c) KPF_6 electrolyte. Surface height maps of Bi/rGO electrode for (d) KPF_6 electrolyte and (e) KFSI electrolyte, and surface potential maps of Bi/rGO electrode for (f) KPF_6 electrolyte and (g) KFSI electrolyte, respectively.

2.5 Mechanical and electrical properties.

The difference of SEI growth mechanism not only result in divergent particle surface chemistries, but also different interactions between the active material and the other electrode components (binder, conductive carbon, current collector), resulting in different mechanical and electrical properties.[51] The mechanical properties of the cycled Bi/rGO electrodes in both electrolytes were measured through nanoindentation tests. The nanoindentation force of the Bi/rGO electrode after 10 cycles in KFSI electrolyte is much lower than that in KPF_6 electrolyte at a given indentation depth (**Figure. 5**(a)), suggesting that the cycled electrode in KFSI is less rigid. The higher viscoelastic property of Bi/rGO electrodes in KFSI electrolyte implies their greater mechanical ability to accommodate the stress generated from the volume changes, and could effectively prevent active material exfoliation and maintain the integrity of the electrode. There is no obvious change for the Bi based electrodes after soaked in both KPF_6 and KFSI electrolytes for 30 days (Figure. S12). However, the electrode materials in the KPF_6 electrolyte peeled off from Cu current collector after 10 cycles, and the separator turned yellowish (Figure. 5(b, c); Figure. S11). In contrast, no obvious change in the separator was observed even after 200 cycles in KFSI electrolyte (Figure. 5 (b, c); Figure. S11). The results further confirmed the better mechanical ability of Bi/rGO electrodes after cycled in KFSI electrolyte. The surface potential of the cycled Bi/rGO electrodes in both electrolytes was measured by Kelvin probe force microscopy (KPFM), a novel microscopic electrical characterization technique that works on the nanoscale (Figure. 5 (d-g), Figure. S13). The surface potential (Vcpd) normally can be defined using formula below:

$$V_{cpd} = (\varPhi_{tip} - \varPhi_{sample})/e$$

Where $\varPhi_{tip}$ and $\varPhi_{sample}$ are the work functions of the tip and sample, respectively, e is the elementary charge.

Based on the contact potential difference method, KPFM was used to map the surface potential of the cycled electrodes, which is expected to change with potassiation and depotassiation. The difference in surface potential between the tip and the sample originates from the difference in the work functions of the electrically connected tip and the sample. Figure. 5 (d, e) shows surface height maps of the Bi/rGO electrodes after 10 cycles in KPF_6 and KFSI electrolytes, respectively. It is obviously observed that the surface of the electrode cycled in KFSI is more uniform, while the surface of the electrode cycled in KPF_6 is rough and thicker, which is in good agreement with the ex-situ SEM results (Figure. S9). Accordingly, their surface potentials are clearly different. The surface potential maps of the cycled Bi/rGO electrodes in both electrolytes are shown in Figure. 5 (f, g). Clearly, the cycled Bi/rGO electrode in KFSI electrolyte has a higher surface potential than the cycled electrode in KPF_6 electrolyte. Since the surface potential represents the contact electrical resistance to a certain extent, the higher surface potential of Bi/rGO electrodes cycled in KFSI electrolyte indicates their higher conductivity and better charge sustaining capacity compared to the electrodes cycled in KPF_6 electrolyte.[54]
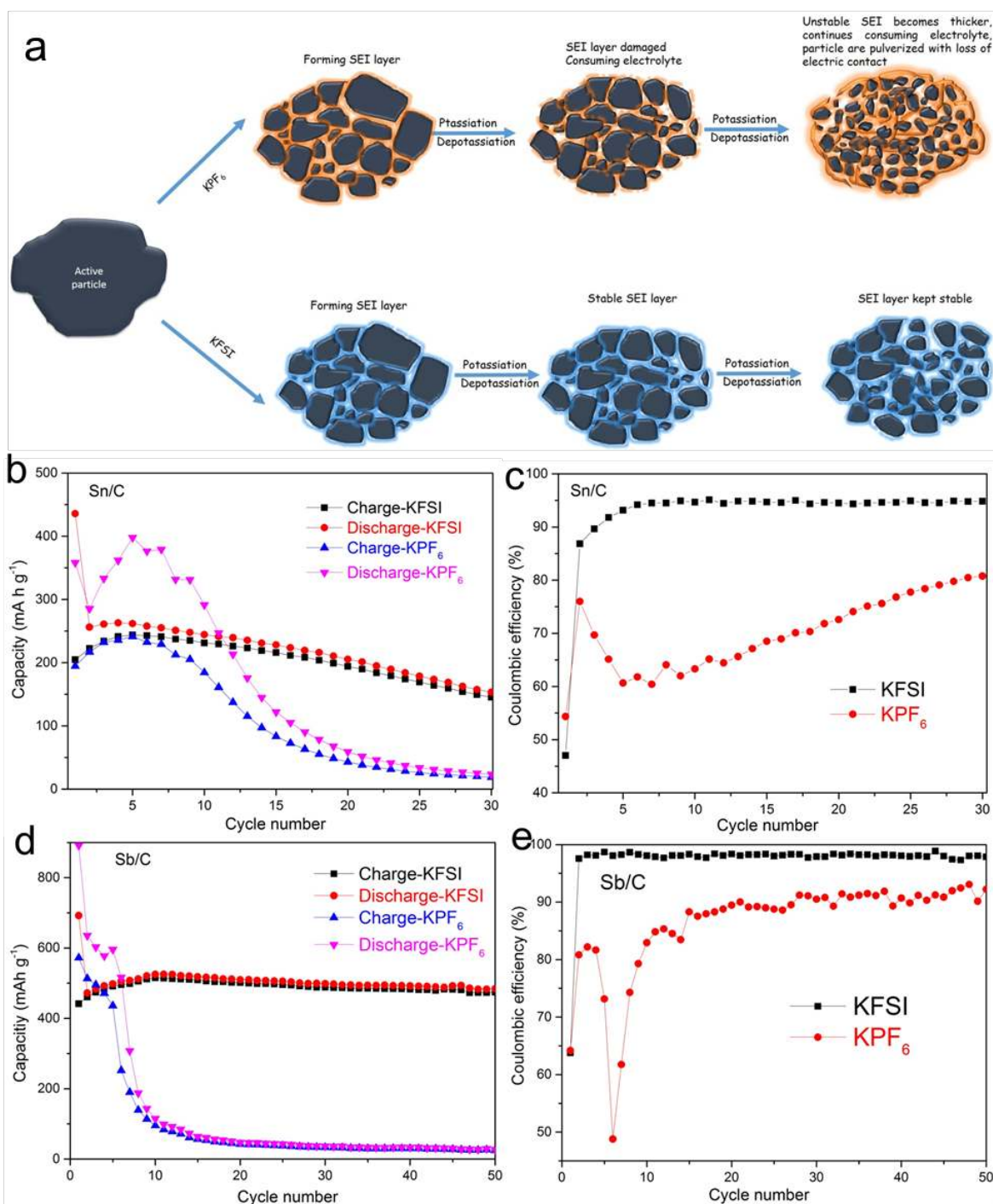
Figure 6. (a) Schematic illustration of the proposed stabilization effects of electrolyte on the SEI layer of Bi/rGO electrode. The cycling performance of (b) Sn/C and (c) Sb/C electrodes in KPF$_6$ and KFSI electrolytes at 50 mA g^{-1}, and the corresponding Coulombic efficiency (d) Sn/C and (e) Sn/C.

2.6 Stabilization effect of electrolyte on the SEI layer and the application on other alloy-based anodes.

Compared to KPF_6, the KFSI induces the generation of a more uniform and stable SEI layer, as well as more favourable interactions between the binder and the active material surface, which contributes to making the surface more conductive, more mechanically robust, and more resistive to solvent penetration. The proposed stabilizing effects of the SEI layer on the active bismuth materials are schematically illustrated in **Figure 6.** (a). The unstable SEI layer in KPF_6 electrolyte could not shield the bulk Bi anode against electrolyte attack, and hence, there is more electrolyte decomposition. In contrast, the stable SEI layer in the KFSI electrolyte has better mechanical and electrical properties, which could effectively suppress the decomposition of the electrolyte, reduce the side reactions, maintain the integrity of the electrode, and thus facilitate the easy transport of K ions through the surface layer formed on the active components. As a result, the Bi anodes in KFSI electrolyte show enhanced electrochemical performance. To demonstrate the general versatility of salt chemistry, both the KFSI and the KPF_6 salts were also employed to test various alloy based anode materials, including Sn/C and Sb/C in PIBs (Figure.S15). The cycling performance and coulombic efficiency (CE) for the Sn/C and Sb/C are shown in Figure 6(b-d). Clearly, both the Sn/C and Sb/C electrodes show fast capacity decay after a few cycles and have almost lost their electrochemical activity after 15 cycles in KPF_6 electrolyte. In contrast, the Sn/C and Sb/C exhibit a capacity of 150 mAh g^{-1} after 30 cycles and 470 mAh g^{-1} after 50 cycles, respectively, in KFSI electrolyte. The CEs of both electrodes in KFSI electrolyte are also higher than in KPF_6 electrolyte. The results further demonstrate the advantages of KFSI salt in carbonate electrolyte for obtaining superior potassium storage performance.

3. Conclusion

In summary, Bi-based materials, including pristine Bi and Bi/rGO nanocomposite were investigated as anodes for potassium-ion batteries. The Bi electrode undergoes a reversible

alloying/dealloying mechanism via a solid-solution and two-phase reactions. Furthermore, a general and convenient strategy has been explored to enhance the electrochemical performance of alloy-based anodes by altering the electrolyte salt. As an example, the experimental investigations on Bi/rGO electrodes demonstrate that the FSI⁻ anion can protect the electrolyte decomposition and modify the surface passivation through the formation of a more uniform, stable, conductive and robust SEI, resulting in better cycling performance. Thus Bi/rGO anodes deliver a high reversible capacity of 290 mAh g^{-1} after 50 cycles when KFSI is used as the salt in carbonate electrolyte. We hope that our work will contribute to further understanding of SEI manipulation and show the way to PIB development via tuning the electrolyte salt.

4. Experimental Section

4.1 Synthesis of graphene oxide.

The graphene oxide was obtained by using a modified Hummers method. Pure graphite (1 g, Sigma-Aldrich, 99.995%) was ground with sodium nitrate (0.5 g, Sigma-Aldrich, ≥ 99.0%), and the mixture was added into concentrated sulfuric acid (50 ml, Sigma-Aldrich, 95.0−98.0%) in a conical flask and stirred in an ice bath. In the following step, potassium permanganate was added (6 g, Sigma-Aldrich, ≥ 99.0%). Then, deionized water was added to reduced the concentration of the solvent mixture. Finally, hydrogen peroxide solution (10 ml, Sigma-Aldrich, ≥ 30.0 wt%) was added into the conical flask dropwise and stirred for 2 hours. The mixture was subjected to ultrasonic processing until a brown homogeneous suspension was formed.

4.2 Synthesis of Bismuth/reduced graphene oxide (Bi/rGO).

Solution A: Bismuth nitrate pentahydrate (2.425 g, Sigma-Aldrich, ≥ 98.0%) was dissolved into 100 ml deionized water, and 20 ml as-prepared graphite oxide (4.0 mg ml^{-1}) was added dropwise and stirred for 30 minutes. Solution B: Potassium borohydride (0.84 g, Sigma-

Aldrich, $\geq$ 98.0%) was dissolved into 100 ml deionized water and stirred for 15 minutes. Solution B was added into Solution A to trigger a redox reaction. The mixture was then stirred for an hour, and the black precipitates were collected by centrifugation and washed several times with deionized water and ethanol. After drying in a vacuum oven at 70° overnight, the target product was finally obtained.

4.3 Synthesis of Sn/C and Sb/C.

Sn/C and Sb/C powders were directly synthesized by ball milling the raw materials, Sn (Aldrich, $\geq$ 99.8%), Sb (Aldrich, $\geq$ 99.5%), and carbon black, respectively. The weight ratios were Sn: C = 77.5: 12.5 and Sb: C = 77.5: 12.5 in the binary composites Sn/C and Sb/C, respectively. The ball milling was conducted in a planetary QM-1SP2 ball mill for 30 h at 500 rpm. A stainless steel jar and stainless steel balls 10 mm in diameter were used. The powder-to-ball weight ratio was 1:30. The storage and handling of all the samples were performed in an Ar filled glovebox (MBraun Unilab).

5. Characterization

5.1 Physical characterization of materials and SEI.

The crystallographic structure of the as-prepared sample and cycled electrodes was characterized by X-ray diffraction (XRD, Science MAC) using Cu Kα radiation at a scanning rate of 1° s^{-1}. Raman spectroscopy was carried out on an instrument (JOBIN YVON HR800) equipped with a 632.81 nm diode laser. The morphological images were acquired by field emission scanning electron microscopy (FESEM, JEOL-7500), transmission electron microscopy (TEM, JEOL-2010), and high resolution (scanning) transmission electron microscopy equipped with EDS (JEOL JEM-ARM200F, 200 kV). Selected area electron diffraction (SAED) patterns were recorded by a Gatan UltraScan 1000XP charge coupled device (CCD) camera. X-ray photoelectron spectroscopy (XPS) was conducted on a VG Multilabel 2000. The vacuum transfer module was used to prevent air exposure.

Thermogravimetric analysis was performed on a TA 2000 Thermoanalyzer. Nanoindentation testing was performed in a UMIS system equipped with a Berkovich diamond indenter with a 100 micrometre tip (E = 1050 GPa). A constant load of 1 mN was applied during the indentation test. Kelvin Probe Force Microscopy (KPFM) measurements were carried out on an MFP-3D AFM instrument (Asylum Research, CA) to measure the morphology and surface potential of the samples. Typically, a Pt/Ir coated silicon probe (EFM, Nanoworld) with resonance frequency of 75 kHz and force constant of 2.8 N m^{-1} was used in the KPFM measurements. The active materials were redispersed in ethanol and distributed on gold Mylar for KPFM measurements. The scan rate was set at 1 Hz under ambient conditions. Before characterizing the surface potential of the samples, the surface potential of the Pt/Ir tip was calibrated on gold Mylar (standard gold). Both KPF_6 and KFSI samples were measured, followed by double-checking on gold Mylar to confirm the consistency of the probe. All KPFM images were generated with a pixel density of 256×256.

5.2 Electrodes Preparation and Electrochemical Measurements.

The electrochemical performance of the materials was tested *via* two-electrode coin half-cells (CR2032). The working electrodes were prepared by mixing the active material with carbon black and sodium carboxymethyl cellulose (CMC) binder in a mass ratio of 80:10:10 in deionized water to form a slurry. The slurry was coated onto the copper foil and dried at 80° overnight under vacuum to eliminate residual solvent, followed by pressing at 300 kg cm^{-2}. The cells were assembled with potassium foil as the counter electrode inside an argon-filled glove box. The electrolyte was 1.0 M potassium bis(fluorosulfonyl)imide (Strem Chemcials Inc., 98.0%) or 0.8 M potassium hexafluorophosphate (Sigma-Aldrich, 99.5%) in ethylene carbonate/diethyl carbonate (EC/DEC, 1:1 v/v). Galvanostatic discharge-charge measurements were conducted on a Land CT2001A battery tester. The voltage window was set in the range of 0.01-1.0 V and 0.01-2.0 V *vs.* K/K$^+$ at different constant current densities.

Cyclic voltammetry (CV) was conducted from 0.01-2.0 V *vs.* K/K$^+$ at 0.05 mV s^{-1} on a Biologic VPM3 electrochemical workstation.

References:

[1]   B. Dunn, H. Kamath, J. M. Tarascon, *Science* **2011**, *334*, 928–935.

[2]   Z. G Yang, J. L. Zhang, M. C. W. Kintner-Meyer, X. C. Lu, D. W. Choi, J. P. Lemmon, J. Liu, *Chem. Rev.* **2011**, *111*, 3577–3613.

[3]   J.M. Tarascon, M. Armand, *Nature* **2001**, *414*, 359–367.

[4]   D. Larcher, J.M. Tarascon, *Nat. Chem.* **2015**, *7*, 19.

[5]   H. L. Pan, Y. S. Hu, L. Q. Chen, *Energy Environ. Sci.* **2013**, *6*, 2338–2360.

[6]   N. Yabuuchi, K. Kubota, M. Dahbi, S. Komaba, *Chem. Rev.* **2014**, *114*, 11636−11682.

[7]   J. Y. Hwang, S. T. Myung, Y. K. Sun, *Chem. Soc. Rev.* **2017**, *46*, 3529−3614.

[8]   X. Wu, D. Leonard, X. Ji, *Chem. Mater.* **2017**, *29*, 5031–5042.

[9]   A. Eftekhari, Z. Jiang, X. Ji, *ACS Appl Mater. Interfaces* **2017**, *9*, 4404–4419.

[10] J. C. Pramudita, D. Sehrawat, D. Goonetilleke, N. Sharma, *Adv. Energy Mater.* 2017, *414*, 1602911.

[11] S. Komaba, T. Hasegawa, M. Dahbi, K. Kubota, *Electrochem. Commun.* **2015**, *60*, 172.

[12] M. Okoshi, Y. Yamada, S. Komaba, A. Yamada, H. Nakai, *J. Electrochem. Soc.* **2017**, *164*, 54–60.

[13] Z. Jian, W. Luo, X. Ji, *J. Am. Chem. Soc.* **2015**, *137*, 11566.

[14] Z. Jian, Z. Xing, C. Bommier, Z. Li, X. Ji, *Adv. Energy Mater.* **2016**, *6*, 1501874.

[15] W. Zhang, J. Mao, S. Li, Z. Chen, Z. P. Guo, *J. Am. Chem. Soc.* **2017**, *139*, 3316–3319.

[16] W. Luo, J. Wan, B. Ozdemir, W. Bao, Y. Chen, J. Dai, H. Lin, Y. Xu, F. Gu, V. Barone, L. B. Hu, *Nano Lett.* **2015**, *15*, 7671-7677.

[17] Z. Jian, S. Hwang, Z. Li, A. S. Hernandez, X. Wang, Z. Xing, D. Su, X. Ji, *Adv. Funct. Mater.* **2017**, *26*, 1700324.

[18] J. Zhao, X. X. Zou, Y. J. Zhu, Y. H. Xu, C. S. Wang, *Adv. Funct. Mater.* **2016**, *26*, 8103–8110.

[19] K. Share, A. P. Cohn, R. Carter, B. Rogers, C. L. Pint, *ACS Nano* **2016**, *10*, 9738–9744.

[20] Y. Li, R. A. Adams, A. Arora, V. G. Pol, A. M. Levine, R. J. Lee, K. Akato, A. M. Naskar, M. P. Paranthaman, *J. Electrochem. Soc.* **2017**, *164*, 1234–1238.

[21] D. S. Bin, Z. X. Chi, Y. T. Li, K. Zhang, X. Z. Yang, Y. G. Sun, J. Y. Piao, A. M. Cao, L. J. Wan, *J. Am. Chem. Soc.* **2017**, *139*, 13492.

[22] K. Lei, F. Li, C. Mu, J. Wang, Q. Zhao, C. Chen, J. Chen *Energy Environ. Sci.* **2017**, *10*, 552–557.

[23] Q. Deng, J. Pei, C. Fan, J. Ma, B. Cao, C. Li, Y. Jin, L. Wang, J. Li, *Nano Energy* **2017**, *33*, 350–355.

[24] X. Ren, Q. Zhan, W. D. McCulloch, Y. Wu, *Nano Res.* **2017**, *10*, 1313–1321.

[25] B. Kishore, G. Venkatesh, N. Munichandraiah, *J. Electrochem. Soc.* **2016**, *163*, 2551–2554.

[26] J. Han, M. Xu, Y. Niu, G. N. Li, M. Wang, Y. Zhang, M. Jia, C. M. Li, *Chem. Commun.* **2016**, *52*, 1274−11276.

[27] Y. Dong, Z. S. Wu, S. Zheng, X. Wang, J. Qin, S. Wang, X. Shi, X. Bao, *ACS Nano* **2017**, *11*, 4792−4800.

[28] M. Naguib, R. A. Adams, Y. Zhao, D. Zemlyanov, A. Varma, J. Nanda, V. G. Pol, *Chem. Commun.* **2017**, *53*, 6883−6886.

[29] W. D. McCulloch, X. Ren, M. Yu, Z. Huang, Y. Wu, *ACS Appl. Mater. Interfaces* **2015**, *7*, 26158−26166.

[30] I. Sultana, T. Ramireddy, M. M. Rahman, Y. Chen, A. M. Glushenkov, *Chem. Commun.* **2016**, *52*, 9279−9282.

[31] V. Lakshmi, Y. Chen, A. A. Mikhaylov, A. G. Medvedev, I. Sultana, M. M. Rahman, O. Lev, P. V. Prikhodchenko, A. M. Glushenkov, *Chem. Commun.* **2017**, *59*, 8272−8275.

[32] I. Sultana, M. M. Rahman, S. Mateti, V. G. Ahmadabadi, A. M. Glushenkov, Y. Chen, *Nanoscale* **2017**, *9*, 3646−3654.

[33] H. Gao, T. F. Zhou, Y. Zheng, Q. Zhang, Y. Q. Liu, J. Chen, H. K. Liu, Z. P. Guo, *Adv. Funct. Mater.* **2017**, *27*, 1702634.

[34] Y.J. Liu, Z. X. Tai, Q. Zhang, H. Q. Wang, W. K. Pang, H. K. Liu, K. Konstantinov, Z. P. Guo, *Nano Energy* **2017**, *35*, 36−43.

[35] N. Xiao, W. D. McCulloch, Y. Wu, *J. Am. Chem. Soc.* **2017**, *139*, 9475–9478.

[36] Y. Gao, Y. Zhao, Y. C. Li, Q. Huang, T. E. Mallouk, D.H. Wang, *J. Am. Chem. Soc.* **2017**, *139*, 15288.

[37] Y. Gao, R. Yi, Y. C. Li, J. Song, S. Chen, Q. Huang, T. E. Mallouk, D.H. Wang, *J. Am. Chem. Soc.* **2017**,*139*, 17359-17367.

[38] K. Xu, *Chem. Rev.* **2004**, *104*, 4303−4417.

[39] C. Vaalma, G. A. Giffin, D. Buchholz, S. Passerini, *J. Electrochem. Soc.* **2016**, *163*, 1295−1299.

[40] C. Wang, L. B. Wang, F. J. Li, F.Y. Cheng, J. Chen, *Adv. Mater.* **2017**, *29*, 1702212.

[41] D. W. Su, S. X. Dou, G. X. Wang, *Nano Energy* **2015**, *12*, 88–95.

[42] X. M. Wang, T. Nishina, I. Uchida, *J. Power Sources* **2002**, *104*, 90−96.

[43] D. Nam, K. Choi, *J. Am. Chem. Soc.* **2017**, *139*, 11055−11063.

[44] W. H. Zuo, W. H. Zhu, D. F. Zhao, Y. F. Sun, Y. Li, J. P. Liu X. W., Lou, *Energy Environ. Sci.* **2016**, *9*, 2881−2891.

[45] J. F. Ni, X. Bi, Y. Jiang, L. Li, J. Lu, *Nano Energy* **2017**, *34*, 356–366.

[46] P. Cucka, C. S. Barrett, *Acta Cryst.* **1962**, *15*, 865.

[47] F. Gascoin, S. C. Sevov, *Inorg. Chem.* **2001**, *40*, 5177-5181.

[48] G. Brauer, E. Zintl, *Zeitschrift für Physikalische Chemie*, **1937**, *37B*, 323-352.

[49] M.Y. Nie B. L. Lucht, *J. Electrochem. Soc.* **2014**, *161*, 1001-1006.

[50] G. G. Eshetu, T. Diemant, S. Grugeon, R. J. Behm, S. Laruelle, M. Armand, S. Passerini, *ACS Appl. Mater. Interfaces* **2016**, *8*, 16087−16100.

[51] B. Philippe, R. Dedryvère, M. Gorgoi, H. Rensmo, D. Gonbeau, K. Edström, *J. Am. Chem. Soc.* **2013**, *135*, 9829−9842.

[52] L. W. Ji, M. Gu, Y. Shao, X. L. Li, M. H. Engelhard, B. W. Arey, W.;Wang, Z. M. Nie, J. Xiao, C. M. Wang, J.G. Zhang, J. Liu, *Adv. Mater.* **2014**, *26*, 2901–2908.

[53] J. M. Zheng, M. H. Engelhard, D. H. Mei, S. H. Jiao, B. J. Polzin, J. G. Zhang, W. Xu *Nat. Energy* **2017**, *2*, 17012.

[54] J. Zhu, K. Y. Zeng, L. Lu, *J. Appl. Phys.* **2012**, *111*, 063723.

Supporting Information
The Supporting Information accompanies this paper is available free of charge on the Wiley Online Library.

Q. Zhang, J. Mao*, W. Pang, T. Zheng, V. Sencadas, Y. Chen, Y. Liu and Z. Guo*

Boosting the potassium storage performance of Alloy-based anode materials via electrolyte salt chemistry

TOC
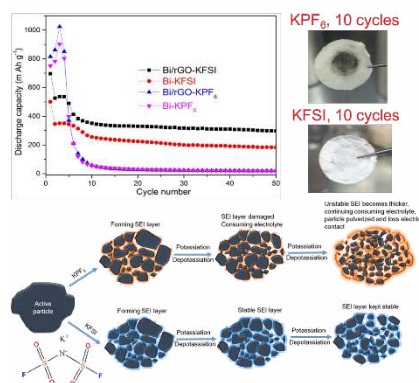
Bismuth stores potassium electrochemically via a solid-solution reaction, followed by two typical two-phase reactions, corresponding to $Bi \leftrightarrow Bi(K)$ and $Bi(K) \leftrightarrow K_5Bi_4 \leftrightarrow K_3Bi$, respectively. Moreover, a more uniform, stable, conductive and robust SEI is achieved by replacing KPF_6 with KFSI, and hence resulted in better cycling performance. The KFSI salt is also effective in other alloy-based anode materials such as Sn and Sb.

Supporting Information

Boosting the potassium storage performance of Alloy-based anode materials via electrolyte salt chemistry

Qing Zhang, Jianfeng Mao*, Wei Kong Pang, Tian Zheng, Vitor Sencadas, Yuanzhen Chen, Yajie Liu and Zaiping Guo*

Qing Zhang, Dr. Jianfeng Mao*, Dr. Wei Kong Pang, Dr. Yuanzhen Chen, Yajie Liu and Prof. Zaiping Guo*
Institute for Superconducting & Electronic Materials, University of Wollongong, Wollongong, NSW 2522, Australia.
E-mail: jmao@uow.edu.au, zguo@uow.edu.au

Dr. Tian Zheng

Intelligent Polymer Research Institute, University of Wollongong, Wollongong, NSW 2522, Australia.

Dr. Vitor Sencadas

School of Mechanical, Materials, Mechatronics & Biomedical Engineering, University of Wollongong, NSW 2500, Australia.

Prof. Zaiping Guo

School of Mechanical, Materials, Mechatronics & Biomedical Engineering, University of Wollongong, NSW 2500, Australia.

Figure S1. Raman spectrum of as-synthesized Bi/rGO composite.
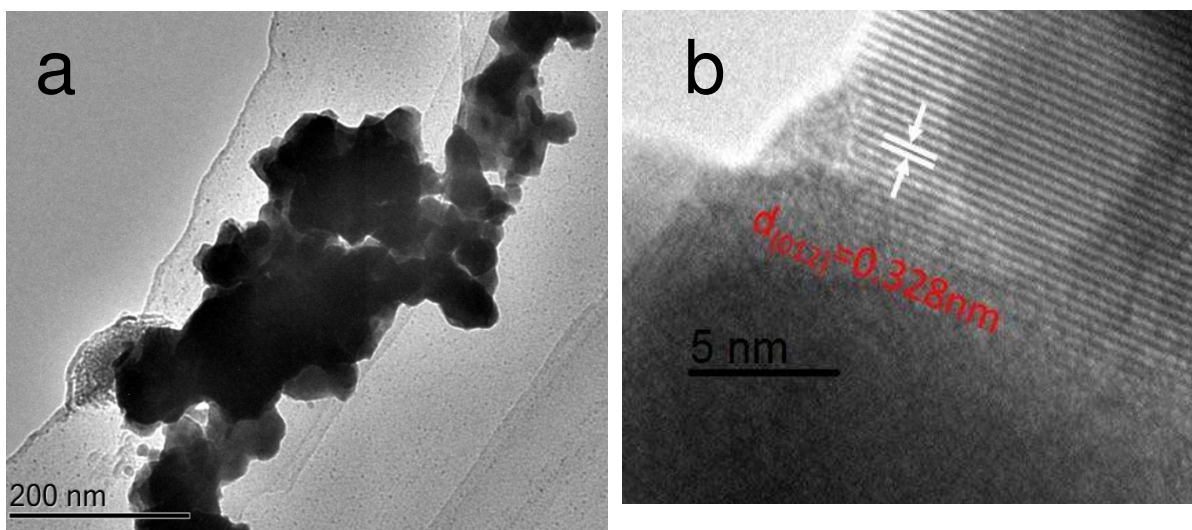
Figure S2. (a) TEM and (b) HRTEM images of as-synthesized Bi.
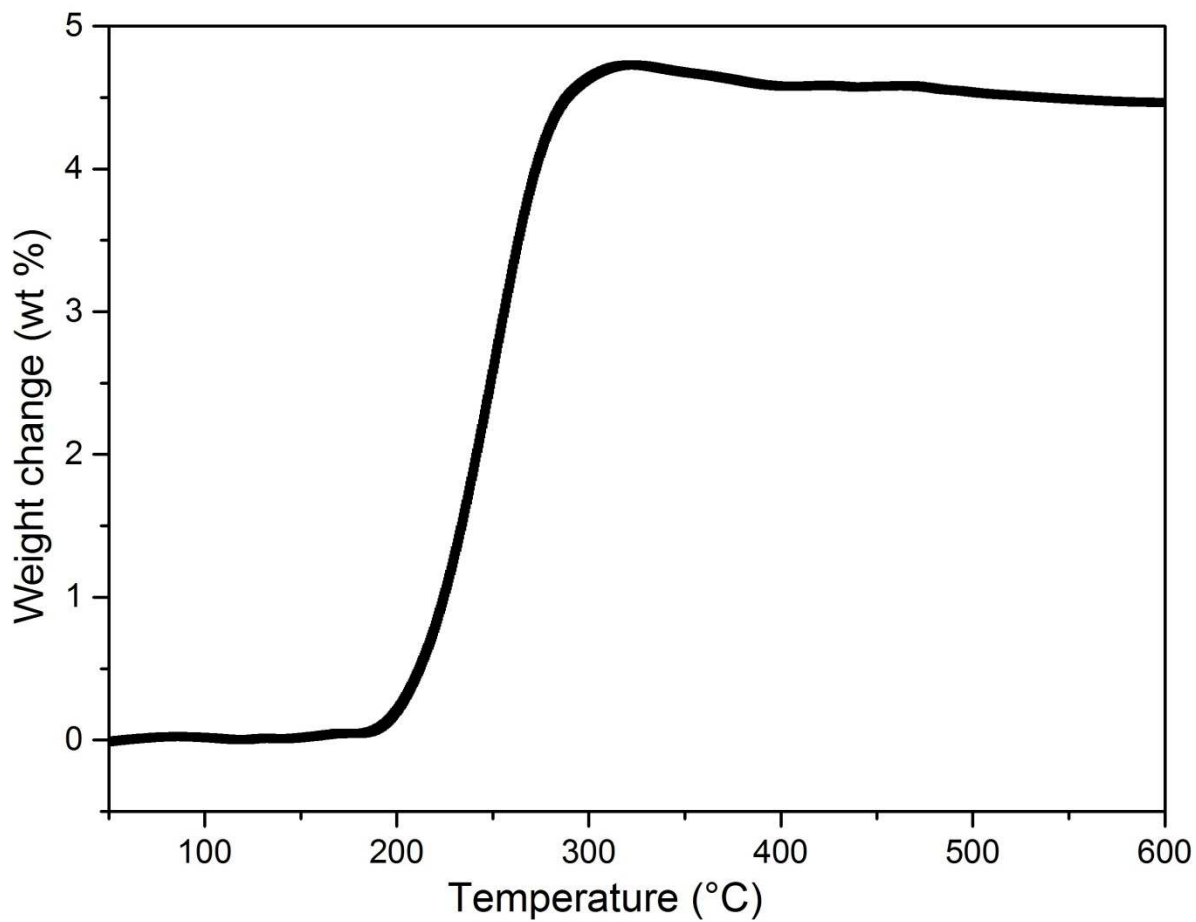
**Figure S3**. Thermogravimetric (TG) analysis curve of Bi/rGO.

Figure S3 presents the TG results for the Bi/rGO composite in air. The weight change is attributed to the oxidation of Bi and C. The oxidation of Bi will lead to an increase in the weight (Bi_2O_3), while the oxidation of C will result in a weight loss.
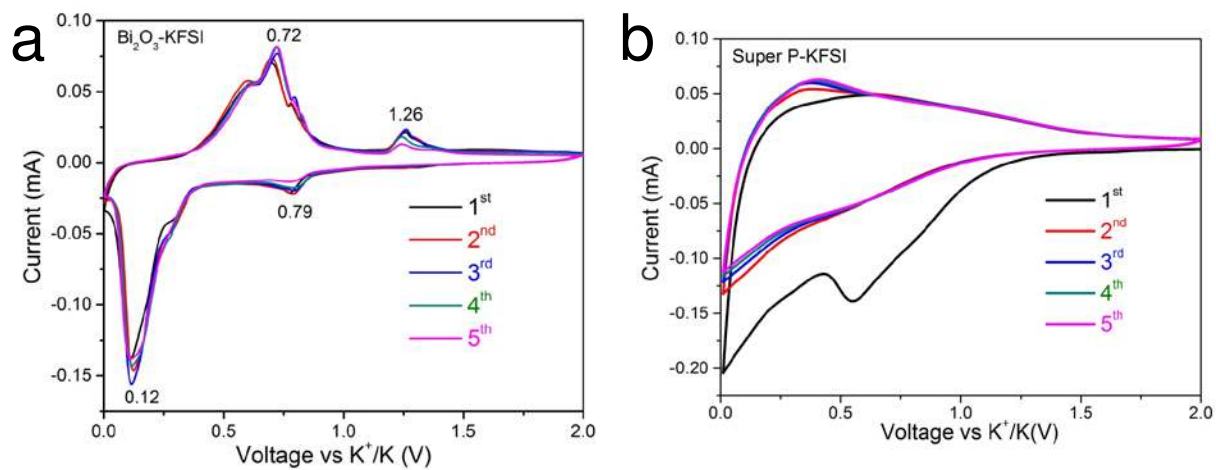
**Figure S4**. CV curves for the first 5 cycles of (a) commercial Bi_2O_3 and (b) carbon black (Super P).
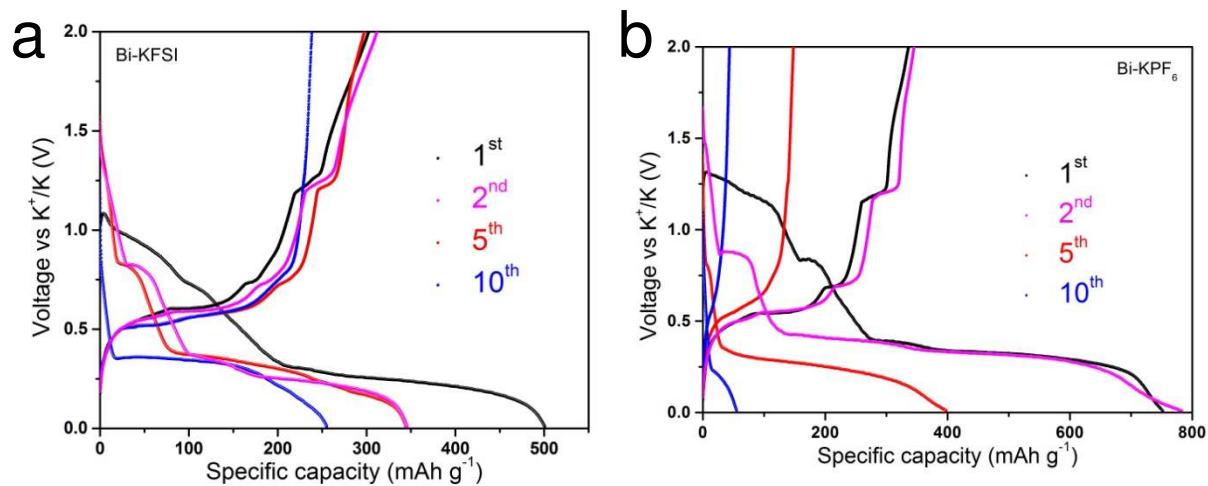
Figure S5. Galvanostatic discharge–charge profiles for selected cycles of the Bi electrode in (a) KFSI electrolyte and (b) KPF$_6$ electrolyte at 50 mA g^{-1}.
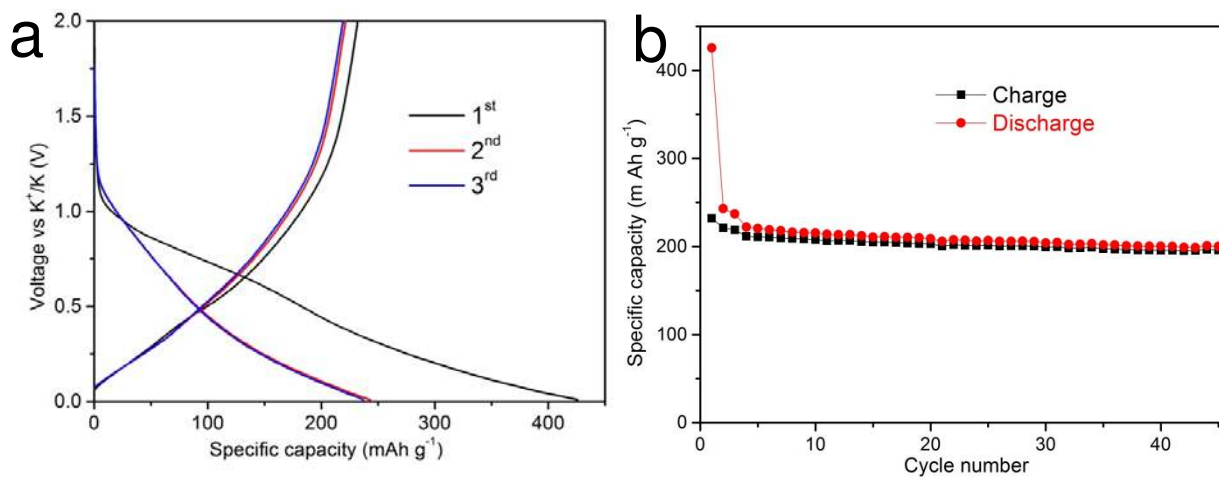
Figure S6. (a) Galvanostatic discharge–charge profiles for the first three cycles of the carbon black, and (b) its cycling performance.
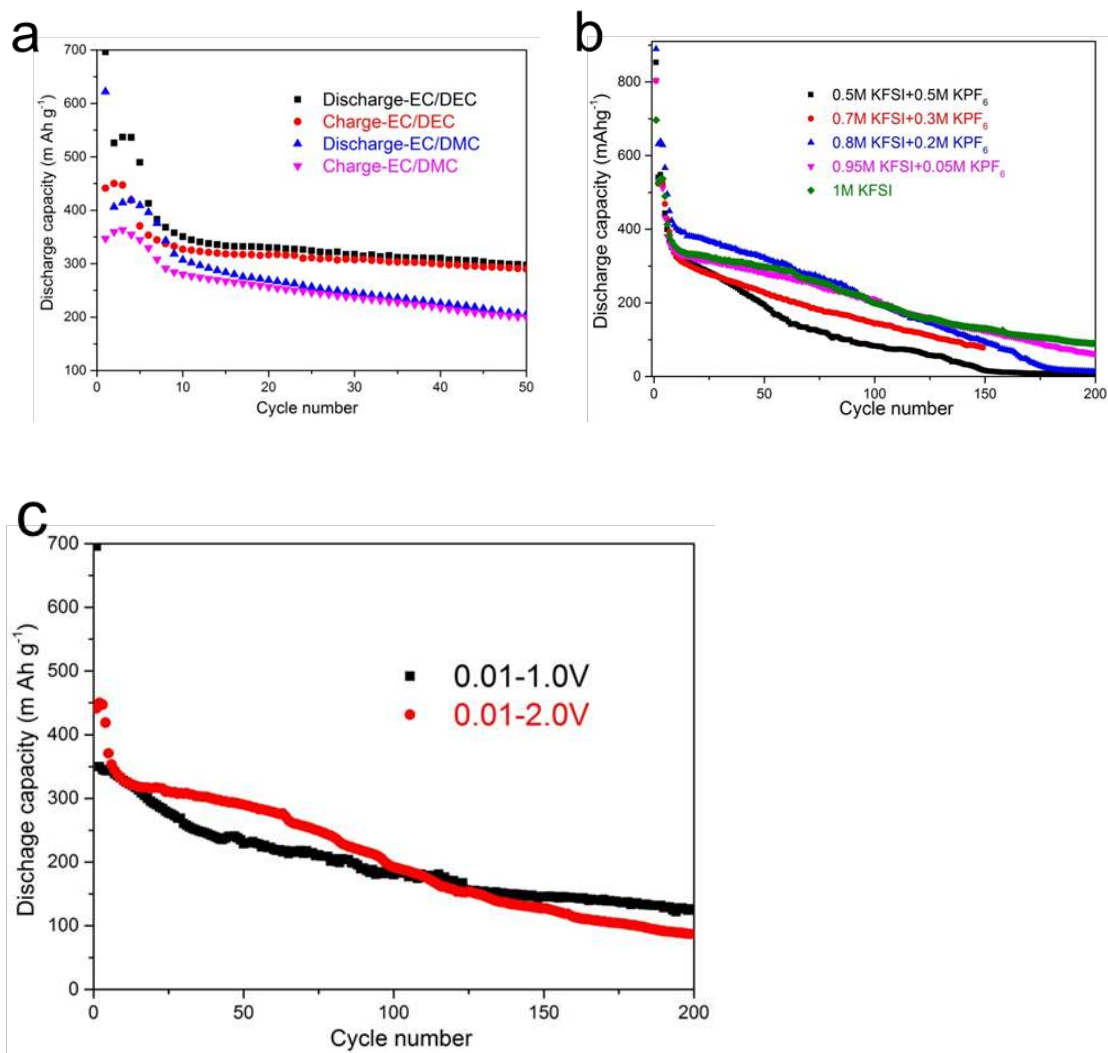
Figure S7. Optimization of the electrochemical performance of Bi/rGO at (a) different combinations of the KFSI and KPF$_6$ salts in EC/DEC, (b) 1M KFSI in EC/DEC and 1 M KFSI in EC/DMC, and (c) 0.01-1 V vs. 0.01-2 V cut-off voltage for electrolyte containing 1 M KFSI in EC/DEC.
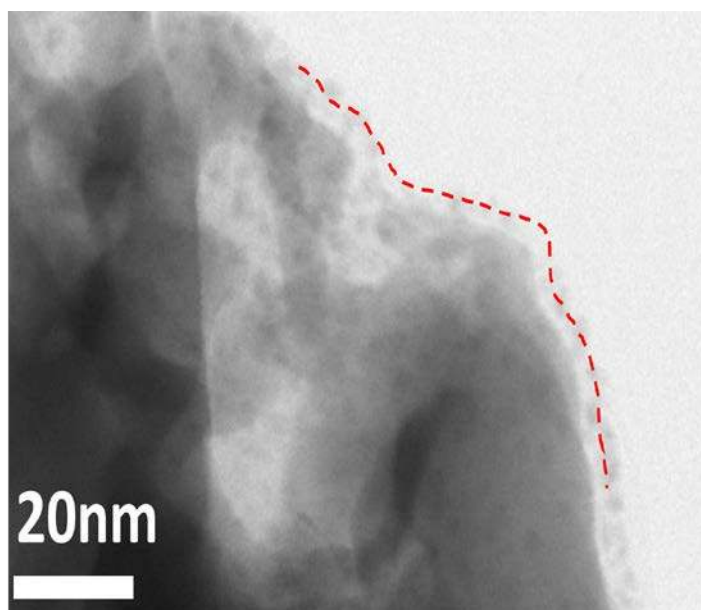
Figure S8. HRTEM image of the SEI layer of Bi/rGO for the 5th cycle in KPF$_6$ electrolyte.
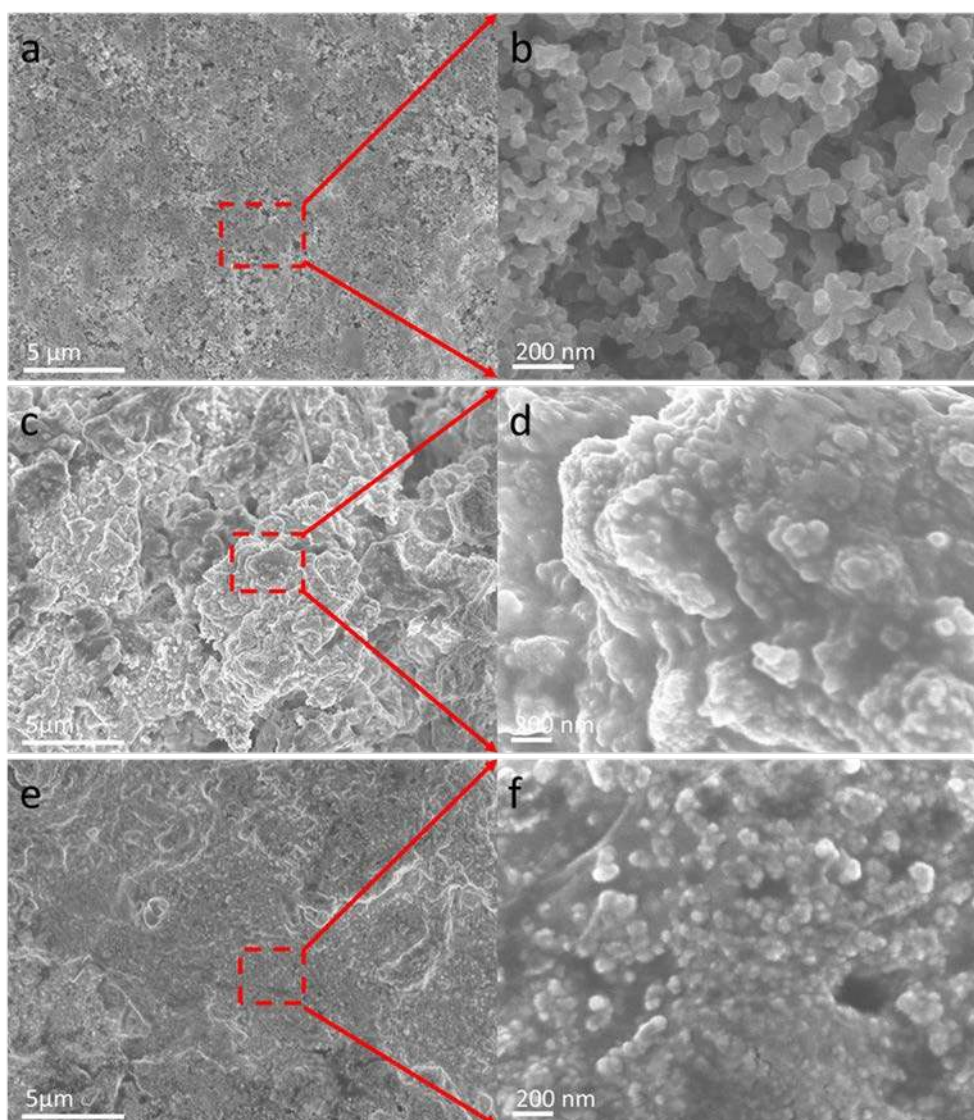
Figure S9. Ex-situ SEM images of Bi/rGO electrodes: a, b) fresh; c, d) after the 10th cycle in KPF_6 electrolyte, and e, f) after the 10th cycle in KFSI electrolyte.

Figure S9 presents the morphology of the Bi/rGO electrodes in the fresh state (a, b) and after 10 cycles in KPF_6 (c, d) and KFSI (e, f) electrolytes. Compared with the pristine electrode, after 10 cycles, the electrode in KPF_6 shows a tremendous change on its surface, and unconnected particles can be detected. In contrast, after 10 cycles, the electrode at KFSI electrolyte remained homogeneous and kept its integrity, with a stable SEI layer uniformly covering the particles.
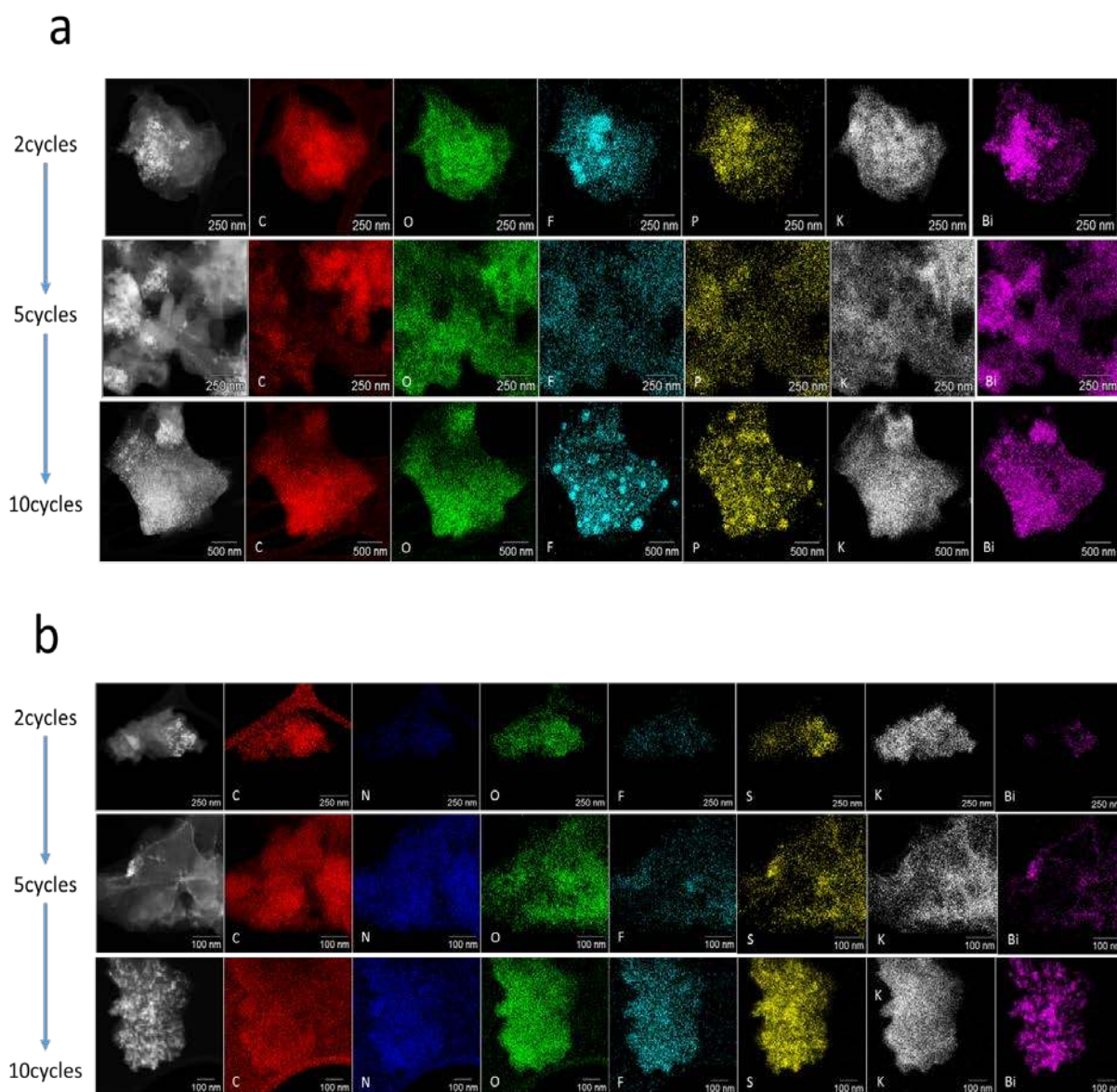
Figure S10. EDS maps of Bi/rGO electrode after 2 cycles, 5 cycles, and 10 cycles in (a) KPF_6 and (b) KFSI electrolytes.

Figure S10 presents energy dispersive spectroscopy (EDS) elemental mapping images of Bi/rGO electrode after 2, 5, and 10 cycles in (a) KPF_6 and (b) KFSI electrolytes. From the images, particular elements from the electrolyte salt (F and P) were clustered in some parts, as shown in Fig. S10a, implied the instability of the SEI in the KPF_6 electrolyte system, while a homogeneous distribution of chemical elements can be observed in Fig S10b, which

indicates that a stable and uniform SEI layer was generated during the cycling process in the KFSI electrolyte system.
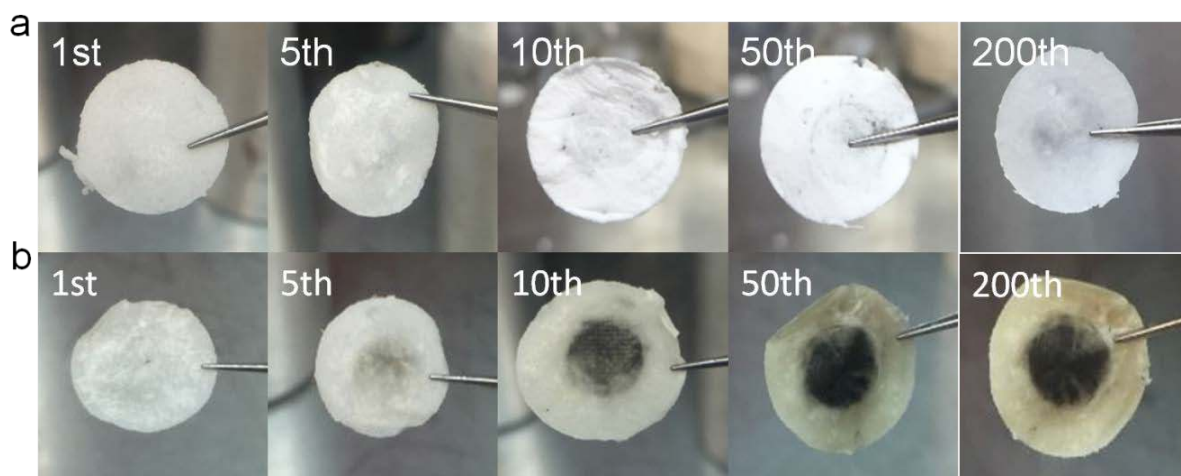

Figure S11. Digital photographs of separators after different numbers of cycles in (a) KFSI electrolyte and (b) KPF$_6$ electrolyte.

It is obvious that the separators in KFSI electrolyte retain their integrity with no colour changes after cycling. In contrast, the separators in KPF$_6$ electrolyte turned yellowish after cycling, indicating that the electrolyte was decomposed. It also can be found that, in KPF$_6$ electrolyte, the active material peels off from the current collector and merges into the separator after only 5 cycles.
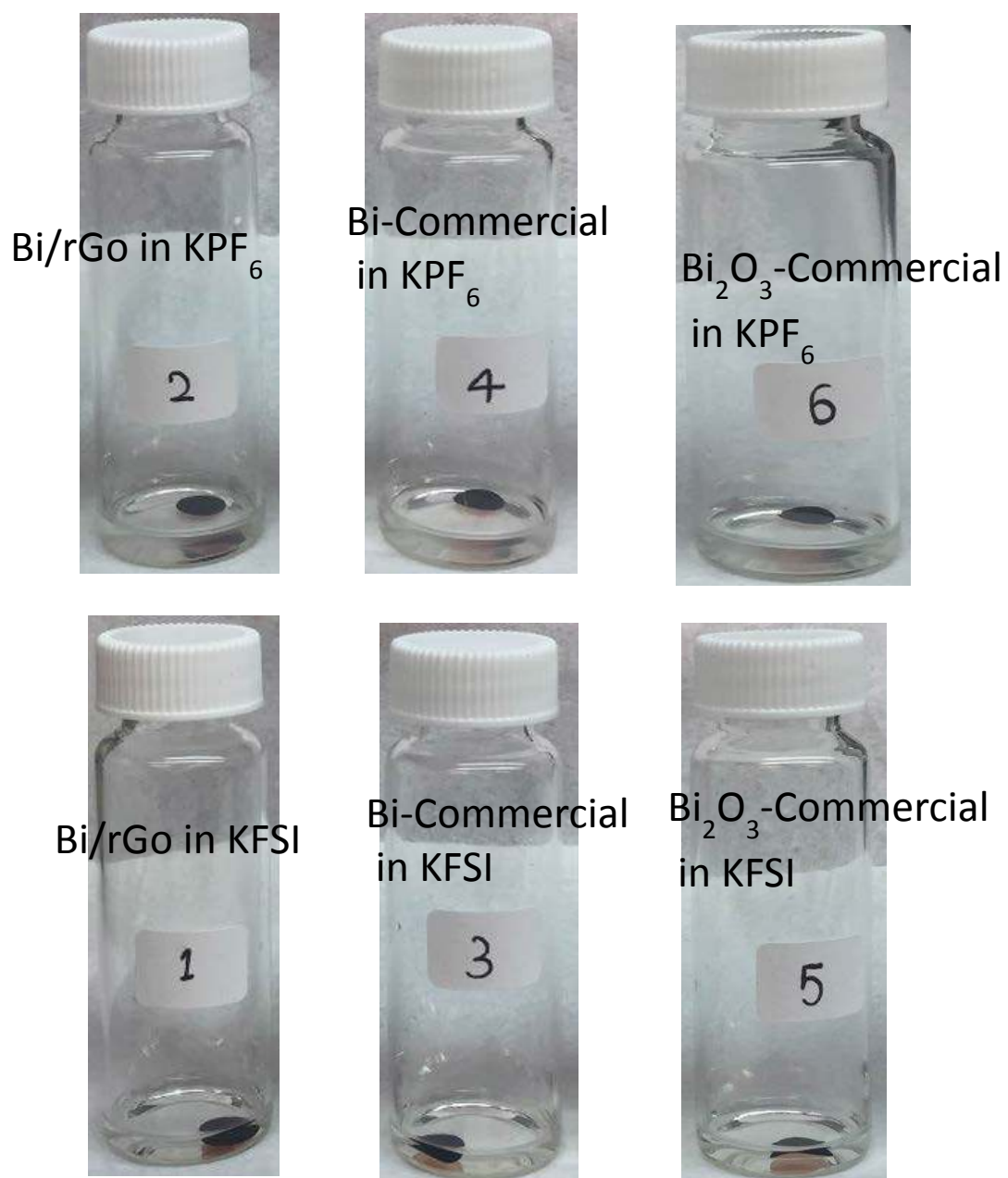
Figure S12. Electrodes soaked in different electrolytes for 30 days.
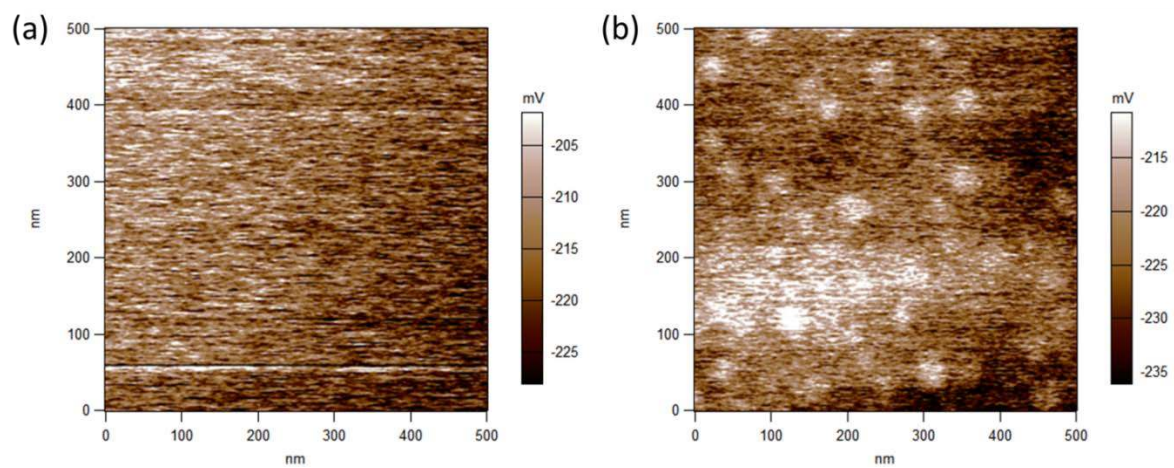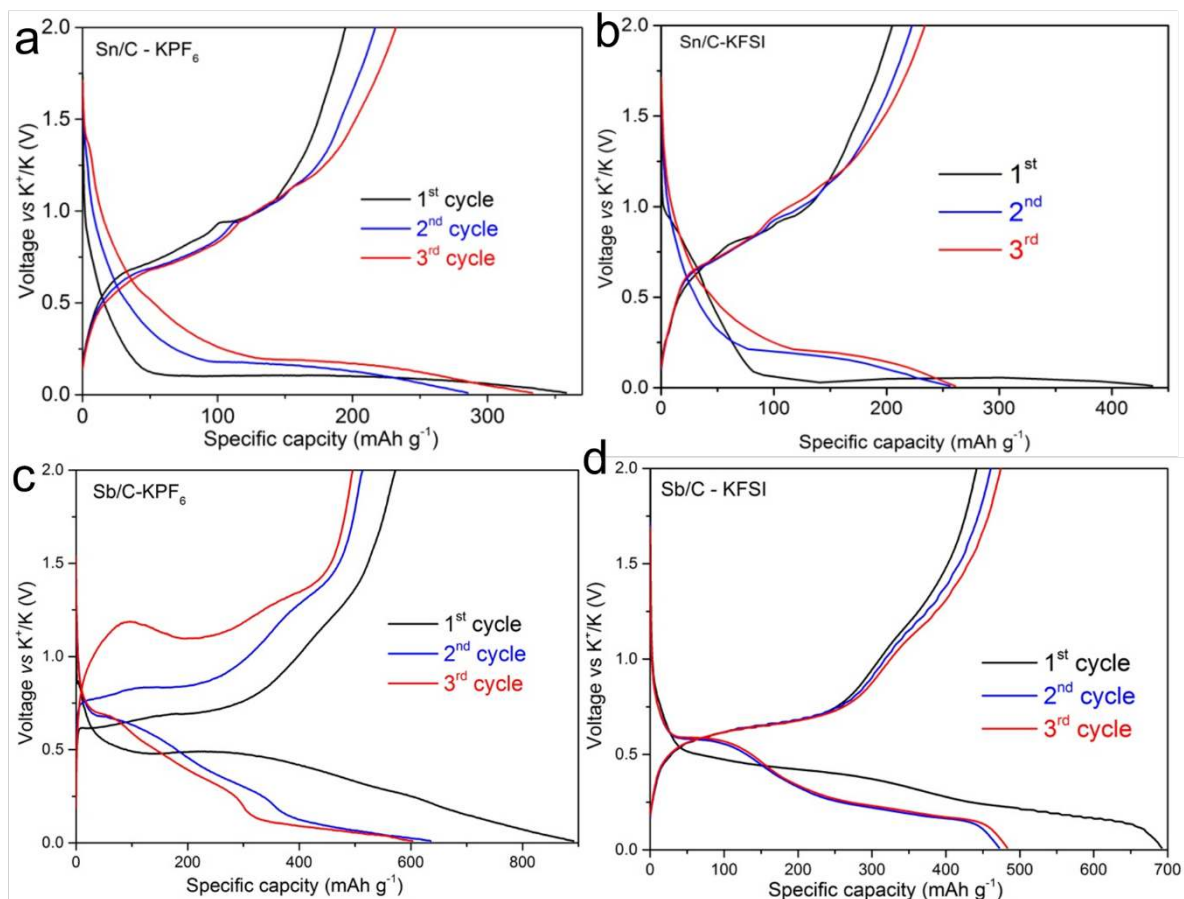
Figure S13. The surface potential map of standard gold Mylar® (a) before and (b) after testing the cycled electrode.
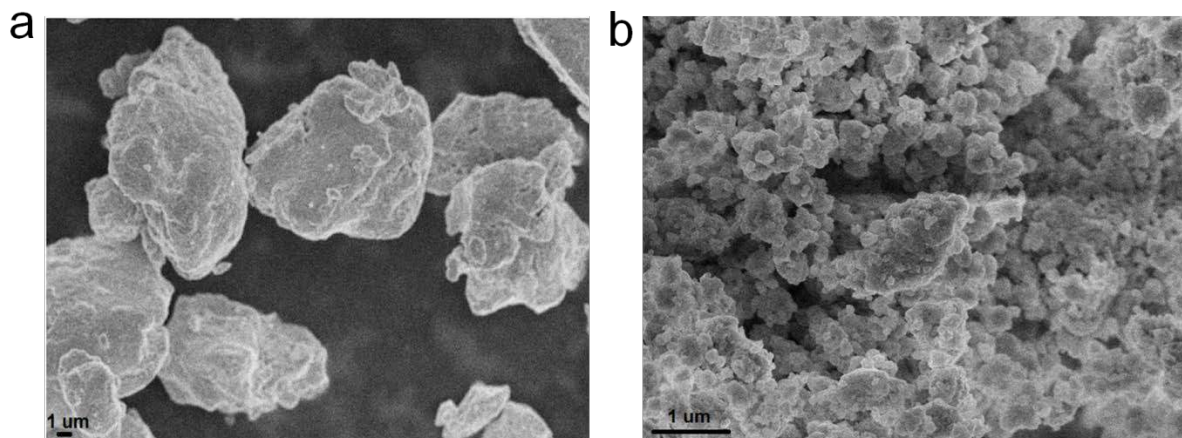
Figure S14. SEM images of of (a) Sn/C and (d) Sb/C electrodes.

The Sn/C powder has irregular agglomerated micrometer sized particles (1-15 μm) (Fig. S14a). The Sb/C powder mainly consists of many irregular crystalline nanoparticles 100-500 nm in size (Fig. S14b).

Figure S15. Galvanostatic discharge–charge profiles for the first 3 cycles of Sn/C and Sb/C electrode in (a) (c) KFSI electrolyte and (b) (d) KPF$_6$ electrolyte at 50 mA g^{-1}, respectively.
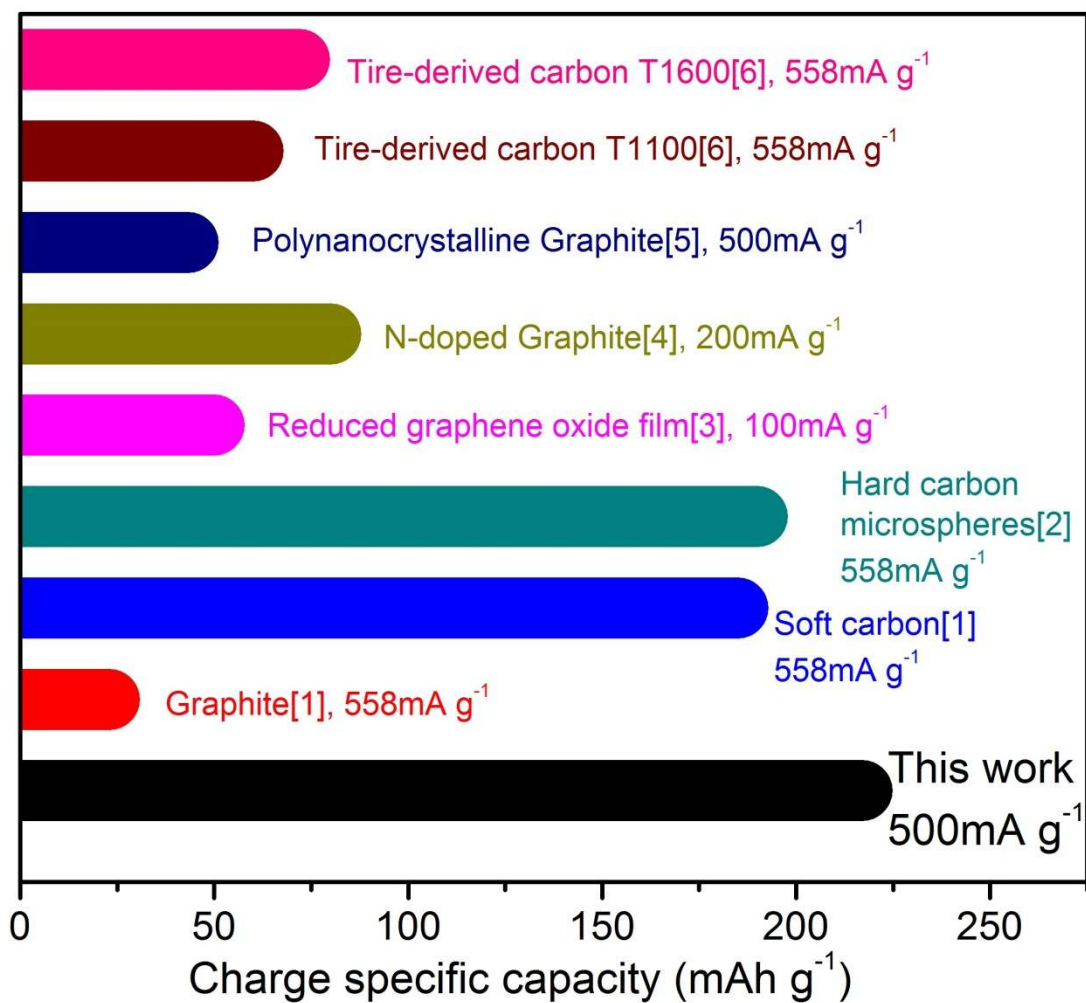
Figure S16. Comparison of the rate performance of our Bi/rGO anode with the reported carbon based anodes. The data are used from Table S1.

Table S1. Comparison of the electrochemical performance of reported anodes for PIBs. The cycling and rate performance of our obtained Bi/rGO was found to be much better than those of most reported anode materials.

Anode Materials	Reversible capacity (mAh g^{-1})				Rate performance (mA g^{-1})	Electrolyte system	Reference
	1st	100th	200th	Current Density (mA g^{-1})			
Bi/rGO	441	192	87	50	217 at 500 mA/g	1 M KFSI in DEC/EC(v/v=1/1)	**This work**
Graphite	197	NA	NA	138.5	23 at 558 mA/g	0.8 M KPF$_6$ in DEC/EC(v/v=1/1)	[1]
Soft carbon	195	NA	NA	558	185 at 558 mA/g		
Hard carbon microspheres	262	216	NA	27.9	190 at 558 mA/g		[2]
Reduced graphene oxide film	165	145	NA	10	50 at 100 mA/g		[3]
N-doped Graphene	270	210	NA	100	80 at 200 mA/g		[4]
Polynanocrystalline Graphite	188	130	100	100	43.2 at 500 mA/g		[5]
Tire-derived carbon T1100	192	160	155	138.5	60 at 558 mA/g		[6]
Tire-derived carbon T1600	181	157	141	138.5	72 at 558 mA/g		
MXene nanosheet Ti$_3$C$_2$	260	50	NA	100	NA	1 M KPF$_6$ in PC/EC(w/w=1/1)	[7]
Titanium carbonitride Ti$_3$CNT$_z$	202	75	NA	20	32 at 500 mA/g	0.8 M KPF$_6$ in DEC/EC(v/v=1/1)	[8]
K$_2$Ti$_4$O$_9$	80	NA	NA	100	56 at 500 mA/g	1 M KPF$_6$ in PC/EC(v/v=1/1)	[9]
K$_2$Ti$_8$O$_{17}$	181.5	NA	NA	20	44.2 at 500 mA/g	0.8 M KPF$_6$ in DEC/EC(v/v=1/1)	[10]
M-KTO(K$_2$Ti$_4$O$_9$)	151	92	NA	50	81 at 300 mA/g	1 M KPF$_6$ in Diglyme	[11]
Sn-C	150	NA	NA	25	NA	0.75 M KPF$_6$ in DEC/EC	[12]
Sn$_3$P$_4$/C	380	50	10	50	258 at 500 mA/g	0.8 M KPF$_6$ in DEC/EC(v/v=1/1)	[13]
SnS$_2$-rGo	355	NA	NA	25	188 at 500 mA/g	0.75 M KPF$_6$ in DEC/EC	[14]
Sb-C	600	NA	NA	NA	434 at 175 mA/g	1 M KPF$_6$ in PC/EC(w/w=1/1)	[15]

Co$_3$O$_4$-Fe$_2$O$_3$-C	420	NA	NA	50	NA	0.75 M KPF$_6$ in DEC/EC(v/v=1/1)	[16]
K$_2$TP	294	240	NA	200	202 at 500 mA/g	1M KPF$_6$ in DME	[17]
K$_2$PC	475	176	NA	44	79 at 440 mA/g	1M KFSI in DMC/EC(v/v=1/1)	[18]
2D Layered MoS$_2$	69	65	64	20	45 at 160 mA/g	0.5 M KPF$_6$ in PC/EC(v/v=1/1)	[19]

References

[1]   Z. Jian, W. Luo, X. Ji, *J Am Chem Soc.* **2015**, *137*, 11566-9.

[2]   Z. Jian, Z. Xing, C. Bommier, Z. Li, X. Ji, *Adv. Energy Mater.* **2016**, *6*, 1501874.

[3]   W. Luo, J. Wan, B. Ozdemir, W. Bao, Y. Chen, J. Dai, H. Lin, Y. Xu, F. Gu, V. Barone, L. B. Hu, *Nano Lett.* **2015**, *15*, 7671-7.

[4]   K. Share, A. P. Cohn, R. Carter, B. Rogers, C. L. Pint, *ACS Nano* **2016**, *10*, 9738-44.

[5]   Z. Xing, Y. Qi, Z. Jian, X. Ji, *ACS Appl. Mater. Interfaces* **2017**, *9,* 4343-4351.

[6]   Y. Li, R. A. Adams, A. Arora, V. G. Pol, A. M. Levine, R. J. Lee, K. Akato, A. M. Naskar, M. P. Paranthaman, *J. Electrochem. Soc.* **2017**, *164*, A1234-A1238.

[7]   X. Yu, Y. Dall'Agnese, M. Naguib, Y. Gogotsi, M. Barsoum, H. Zhuang, P. Kent, *ACS Nano* **2014**, *8*, 9606-9615.

[8]   M. Naguib, R. A. Adams, Y. Zhao, D. Zemlyanov, A. Varma, J. Nanda, V. G. Pol, *Chem. Commun.* **2017**, *53*, 6883-6886.

[9]   B. Kishore, V. G, N. Munichandraiah, *J. Electrochem. Soc.* **2016**, *163*, A2551-A2554.

[10] J. Han, M. Xu, Y. Niu, G. Li, M. Wang, Y. Zhang, M. Jia, C. Li, *Chem. Commun.* **2016**, *52*, 11274-11276.

[11] Y. Dong, Z. S. Wu, S. Zheng, X. Wang, J. Qin, S. Wang, X. Shi, X. Bao, *ACS Nano* **2017**, *11*, 4792-4800.

[12] I. Sultana, T. Ramireddy, M. M. Rahman, Y. Chen, A. M. Glushenkov, *Chem.*

Commun. **2016**, *52*, 9279-82.

[13]   W. Zhang, J. Mao, S. Li, Z. Chen, Z. P. Guo, *J. Am. Chem. Soc*. **2017**, *139*, 3316-3319.

[14]   V. Lakshmi, Y. Chen, A. A. Mikhaylov, A. G. Medvedev, I. Sultana, M. M. Rahman, O. Lev, P. V. Prikhodchenko, A. M. Glushenkov, *Chem. Commun.* **2017**, *53*, 8272-8275.

[15]   W. D. McCulloch, X. Ren, M. Yu, Z. Huang, Y. Wu, *ACS Appl. Mater. Interfaces* **2015**, *7*, 26158-66.

[16]   I. Sultana, M. M. Rahman, S. Mateti, V. G. Ahmadabadi, A. M. Glushenkov, Y. Chen, *Nanoscale* **2017**, *9*, 3646-3654.

[17]   K. Lei, F. Li, C. Mu, J. Wang, Q. Zhao, C. Chen, *Energy Environ. Sci.* **2017**, *10*, 552-557.

[18]   Q. Deng, J. Pei, C. Fan, J. Ma, B. Cao, C. Li, Y. Jin, L. Wang, J. Li, *Nano Energy* **2017**, *33*, 350-355.

[19]   X. Ren, Q. Zhan, W. D. McCulloch, Y. Wu, *Nano Research* **2017**, *10*, 1313-1321.